Hypoxia compromises the mitochondrial metabolism of Alzheimer's disease microglia *via* HIF1

Rosana March-Diaz[1,†], Nieves Lara-Ureña[1,†], Carmen Romero-Molina[1,2,3,†], Antonio Heras-Garvin[1,4,†], Clara Ortega-de San Luis[1,5,†], Maria I. Alvarez-Vergara[1], Manuel A. Sanchez-Garcia[1,6], Elisabeth Sanchez-Mejias[2,7], Jose C. Davila[2,7], Alicia E. Rosales-Nieves[1], Cristina Forja[1], Victoria Navarro[1,2,3], Angela Gomez-Arboledas[2,7], Maria V. Sanchez-Mico[1,2,3], Adrian Viehweger[1,8], Almudena Gerpe[9], Emma J. Hodson[10], Marisa Vizuete[1,2,3], Tammie Bishop[10], Alberto Serrano-Pozo[11], Jose Lopez-Barneo[1,2], Edurne Berra[9], Antonia Gutierrez[2,7], Javier Vitorica[1,2,3,*], and Alberto Pascual[1,*]

[1]Instituto de Biomedicina de Sevilla (IBiS), Hospital Universitario Virgen del Rocio/CSIC/Universidad de Sevilla. 41013 Seville, Spain.
[2]Centro de Investigacion Biomedica en Red sobre Enfermedades Neurodegenerativas (CIBERNED), Madrid, Spain.
[3]Dept. Bioquimica y Biologia Molecular, Facultad de Farmacia, Universidad de Sevilla.
[4]Current address: Division of Neurobiology, Department of Neurology, Medical University of Innsbruck, 6020, Innsbruck, Austria.
[5]Current address: School of Biochemistry and Immunology, Trinity Biomedical Sciences Institute, Trinity College of Dublin, D2 Dublin, Ireland.
[6]Current address: Medical Research Council Centre for Inflammation Research, The Queen's Medical Research Institute, The University of Edinburgh, EH16 4SA, Edinburgh, United Kingdom.
[7]Dept. Biologia Celular, Genetica y Fisiologia. Facultad de Ciencias. Instituto de Investigacion Biomedica de Malaga–IBIMA. Facultad de Ciencias, Universidad de Malaga, Malaga, Spain.
[8]Current address: Dept. of Pediatric Radiology. University Clinic Leipzig. 04103 Leipzig, Germany.
[9]CIC bioGUNE-BRTA (Basque Research and Technology Alliance), 48160 Derio, Spain.
[10]Target Discovery Institute, NDM Research Building, OX3 7FZ Oxford, UK.
[11]Department of Neurology of the Massachusetts General Hospital, Harvard Medical School, Boston, MA, USA.
[†]These authors contributed equally.
*These authors jointly supervised this work.
Correspondence to: apascual-ibis@us.es or vitorica@us.es
Short title: **HIF1 and AD microglial dysfunction**
Keywords: Hypoxia, Alzheimer's disease, microglia, HIF1, aerobic respiration, anaerobic glycolysis.

Abstract

Genetic Alzheimer's disease (AD) risk factors associate with reduced defensive Aß plaque-associated microglia (AßAM), but the contribution of modifiable AD risk factors to microglial dysfunction is unknown. In AD mouse models, we observe the concomitant activation of the HIF1 pathway and the transcription of mitochondrial-related genes in AßAM, and the elongation of mitochondria, a cellular response to maintain aerobic respiration under low nutrient and oxygen conditions. Overactivation of HIF1 induces microglial quiescence *in cellulo* with lower mitochondrial respiration and proliferation. *In vivo*, overstabilization of HIF1, either genetically or by exposure to systemic hypoxia, reduces AßAM clustering and proliferation and increases Aß neuropathology. In the human AD hippocampus, the upregulation of HIF1α and HIF1 target genes correlates with reduced Aß plaques microglial coverage and the increase of Aß plaque-associated neuropathology. Thus, hypoxia, a modifiable AD risk factor, hijack microglial mitochondrial metabolism and converge with genetic susceptibility to cause AD microglial dysfunction.

Introduction

In 1919, Pío del Río-Hortega grouped several morphologic entities of the central nervous system under the term "microglia"[1] (see[2] for a commented English translation), showing that microglia could adapt to changing environments by activating migration, proliferation, growth, and phagocytosis.

In Alzheimer's disease (AD), microglia adapt their morphology and function to cluster and establish a protective barrier around senile plaques[3]. Increasing evidence implicates the decline of microglial defensive responses in the progression of the disease: (1) Single-nucleotide polymorphisms in several genetic *loci* encoding proteins with known roles in innate immunity are associated with an increased risk of developing AD[4]; (2) functional studies of AD-related polymorphisms suggest that microglia play a protective role in AD, which is altered by these individual loss of function genetic variants[5]; and (3) post-mortem studies in AD brains have reported that microglial cells acquire a dysfunctional phenotype[6], degenerate[7], and die by apoptosis[8], thereby contributing to the deposition of Aß and the development of plaque-associated dystrophic neurites[3,9–11].

But, why do AD microglia become dysfunctional? Aß activates a plethora of signaling pathways, which converge in a common microglial neurodegenerative phenotype (MGnD) observed in all the disease-associated microglia (DAM)[12,13]. Loss of function of genetic AD risk factors, such as the triggering receptor expressed on myeloid cells 2 (TREM2) and the apolipoprotein E (APOE), are associated with microglial dysfunction characterized by reduced clustering and survival around Aß plaques[9,11,14,15]. Based on those data, it has been suggested that microglial activation may not only be required to protect against neurodegeneration but also to avoid a low-energy state induced by the disease[16].

Microglia are the brain cells able to survive closer to Aß plaques[17] and an upregulation of the hypoxia-inducible factor 1 (HIF1), the master regulator of oxygen homeostasis[18], has been suggested in Aß plaque-associated microglia (AßAM)[16,19], indicating local low oxygen levels. In addition to non-modifiable genetic risks, there are also potentially modifiable AD risk factors that together strongly contribute to the onset of dementia[20,21], by accelerating the progression of the disease through multiple mechanisms. Several of these factors (e.g. hypertension, obesity, atrial fibrillation, diabetes mellitus, physical inactivity, and smoking) converge in altering the

vascular system and/or reducing oxygen/nutrient availability[20–22]. We hypothesize that local clues synergize with systemic diseases progressing with hypoxia to activate HIF1 and compromise microglial function.

Results

The HIF1-mediated stress response pathway is induced in AßAM

The mRNA levels of *Hif1a* and several HIF1 targets, including those involved in anaerobic glycolysis (glucose to lactate), are suspected to be upregulated in DAM[16,19]. The switch from aerobic respiration to anaerobic glycolysis has been proposed as a metabolic adaptation to sustain DAM energy demand[23] but also a detrimental event[19]. Therefore, we investigated the contribution of HIF1 to AßAM transcription. We first showed that *Hif1a* mRNA is expressed around Aß plaques in an AD mouse model (Fig. 1a). We then combined *in situ* hybridization (ISH) with immunofluorescence for the microglial ionized calcium-binding protein (IBA1) and revealed that AßAM also expressed high *Hif1a* mRNA levels (Fig. 1a), whereas low expression levels were observed in microglia distal to Aß deposits and from WT mice (Fig. 1a, b). To further investigate if *Hif1a* mRNA upregulation has functional consequences over AßAM transcription, we used the transcription factor enrichment analysis (TFEA.ChIP)[24]. We found that HIF1α and HIF2α were among the top proteins predicted as regulators of *APP-PSEN1/+* microglial transcription (Fig. 1c and Supplementary Table 1), suggesting a preponderant role of HIF-mediated transcription in AßAM.

To formally demonstrate a HIF1-dependent transcriptional activation in AßAM, we defined the HIF1/hypoxia-induced microglial module (HMM) using a transcriptomic analysis of primary microglial cell cultures exposed to hypoxia or normoxia (hypoxia: 1% O_2; 6 h *versus* normoxia: 21% O_2; 6 h): we first checked that our cultures were enriched in microglia using immunofluorescence (Extended Data Fig. 1a) and qRT-PCR (Extended Data Fig. 1b), performed principal component analysis (Extended Data Fig. 1c), identified the differentially expressed (DE) genes (Fig. 1d and Supplementary Tables 2–3), validated the DE genes by qRT-PCR (Extended Data Fig. 1b), and demonstrated their regulation by HIF1 using the inducible Cx3cr1-Cre::ESRT2-mediated deletion of *Hif1a* in primary microglial cultures (Fig. 1e, f). We then studied the transcriptional profile of isolated microglia from an Aß plaque-depositing (*APP$_{751}$SL/+* –APP–) and a non-depositing *MAPT*p.P301S/+ (TAU) mouse model. To this end, we developed a protocol based in the sorting of CD11b reactive ($^+$)/CD45$^+$ microglia into CLEC7a$^+$ (strongly expressed by DAM[13,25,26]) and negative (homeostatic) subpopulations (Extended Data Fig. 2a–e for the gating strategy employed). CLEC7a-reactive microglia were

increased in 12-month-old APP and end-stage TAU mice (pathologic state), but remained unaltered in age-matched wild-type (WT) or 3-month-old AD models (pre-pathologic state; Extended Data Fig. 2f). Global gene expression profile studies (Extended Data Fig. 2g and Supplementary Table 4) followed by gene set enrichment analysis (GSEA) revealed that pathologic state APP microglia showed a strong enrichment of the HMM (Fig. 1g) while the TAU model presented only a mild induction (Extended Data Fig. 1e and Supplementary Table 5), despite a similar MGnD[26] gene set (GS) (Supplementary Table 6) enrichment in both models (Fig. 1g, Extended Data Fig. 1e and Supplementary Table 5), indicating a similar degree of activation. Direct comparison of the differentially expressed genes between APP and TAU pathologic state microglia revealed the HMM as the most enriched GS in APP (Extended Data Fig. 1f and Supplementary Table 5), although these two experimental models had similar global transcription profiles (Extended Data Fig. 2g; Supplementary Table 5).

Then, we investigated whether the HIF1 pathway was also upregulated in other DAM. We reanalysed the global expression profile data of microglia isolated form other neurodegenerative or aging models using CD45/CD11b markers[27–29]. Expectedly, the MGnD GS was activated in microglia from all models (Extended Data Fig. 1g and Supplementary Table 7), whereas the HMM was a prominent characteristic of the AßAM (Extended Data Fig. 1h and Supplementary Table 7) and was found only modestly upregulated in others DAM (Supplementary Table 7), suggesting that AßAM may be metabolically challenged by low oxygen levels.

Increased OXPHOS-related transcription in AD microglia

HIF1-mediated transcriptional program normally induces a metabolic switch from aerobic mitochondrial respiration to anaerobic glycolysis[18]. Paradoxically, the oxidative phosphorylation (OXPHOS) GS was dramatically enriched in both Aß and TAU neurodegenerative mouse models (Fig. 2a, Extended Data Fig. 3a, and Supplementary Tables 5 and 7), including upregulation of the mRNA levels of genes encoding proteins for all the mitochondrial electron transport chain complexes (Complex I to IV) and the complex V (ATPase) (Fig. 2a and Extended Data Fig. 3a). Those data were confirmed by the enrichment of other GSs implicated in aerobic respiration and ATP production (Fig. 2b). Moreover, GSs related to antiviral responses and aerobic respiration represented around 50% of the top GSs enriched in DAM (Extended Data Fig. 3b and Supplementary Table 5). Finally, we verified that OXPHOS GS was

enriched in DAM from all the neurodegenerative models and, somehow surprisingly, substantially reduced in the microglia from aged mice (Extended Data Fig. 3c and Supplementary Table 7).

To corroborate that our results were also relevant for the human disease, we interrogated the data from a recent human single cell RNAseq study[30]. Microglia isolated from post-mortem human AD samples clustered in two groups differentiated from Control microglia (Fig. 2c) and the genes encoding the OXPHOS were significantly overexpressed in microglial cells from AD samples (Fig. 2c).

The OXPHOS upregulation constitutes a *bone fide* indicator of mTOR biosynthetic activity *via* mitochondrial activation[31], a pathway that has been described as regulated by TREM2[16]. Interestingly, we reanalysed the data from[16] and observed that TREM2 deficiency is indeed associated with a dramatic downregulation of the OXPHOS GS in microglia from the *5xfAD*/+ mouse model (Fig. 2d and Supplementary Table 9), suggesting that TREM2 activates OXPHOS transcription in AßAM. Induction of protein synthesis, another mTOR activation landmark[32], was highly enriched in AßAM (Extended Data Fig. 3b and Supplementary Table 5). So, we also interrogated our transcriptomic data for the presence of an mTOR signature[16] (Supplementary Table 8) and found a modest enrichment in both the Aß and TAU models (Extended Data Fig. 3d).

Altogether, those data strongly indicate that an increase in the transcription of the aerobic respiration-related genes is taking place both in AD mouse models and human AD microglia in a TREM2 dependent manner.

AßAM mitochondria are characterized by elongation

We have demonstrated that the AßAM is characterized by simultaneous activation of two antagonistic pathways: (i) the HIF1 pathway (a classical trigger of anaerobic glycolysis[18]) (Fig. 1 and Extended Data Fig. 1) and (ii) aerobic respiration (Fig. 2 and Extended Data Fig. 3). We have also shown that the HIF1 pathway is particularly enriched in AßAM *versus* other DAM (Fig. 1 and Extended Data Fig. 1). This peculiar metabolic adaptation of AßAM suggests that mitochondrial activity is essential for microglial metabolic fitness in response to Aß and that HIF1 activation could be an unwanted by-product of the chronic defensive activity of innate immune cell clusters (only present in Aß-depositing mouse models). In addition, a reduction of

the vasculature around Aß plaques has been consistently reported in the literature in both the human AD brain and AD mouse models[22,33], that could also contribute to the high HIF1 activation. To better understand this paradoxical situation, we search for situations where mitochondrial activity is preserved despite HIF1 activation and found that cells under nutrient and oxygen deprivation prevent a HIF1-mediated switch to anaerobic glycolysis by elongating mitochondria[34], a well-described process that optimizes aerobic ATP production and prevents mitophagy[35]. Therefore, we first evaluated mitochondrial levels by immunofluorescence, and observed a clear upregulation of NDUFS2 complex I protein in AßAM when compared with wilt-type or distal to Aß plaques microglia (Fig. 3a). As AßAM phagocyte other cells and are in close apposition with dystrophic neurites that also contain mitochondria, we investigated the morphology of AßAM mitochondria using electron microscopy. Microglia distant from Aß plaques presented round-shaped mitochondria (Fig. 3b), but AßAM showed elongated mitochondria surrounded by rough endoplasmic reticulum (Fig. 3c), characterized by increased perimeter and aspect ratio, and decreased circularity versus Aß plaque distal or WT microglia (Fig. 3d).

Altogether, these results indicate that aerobic respiration is a common feature of neurodegenerative DAM, while the concomitant activation of HIF1-mediated gene expression and the elongation of their mitochondria suggest that AßAM metabolism is compromised.

Overactivation of HIF1 induces microglial quiescence

To verify that activation of microglia depends on mitochondrial activity, we treated microglial cell primary cultures with oligomeric Aß (oAß) for 24 h and measured the mitochondrial O_2 consumption rate. Interestingly, 24 h after stimulation, a clear up-regulation of the mitochondrial maximal respiratory capacity was observed (Fig. 4a), that was accompanied with a slight but significant increase in the mitochondrial protein SDHA (Complex II), a trend to increase in NDUFS2 (Complex I; Fig. 4b), and no changes in ATPsynß (Complex V; Fig. 4b). oAß also induced the microglial response characterized by the increase of *Tnf* and *Il6* mRNA levels (Fig. 4c). Altogether, our data indicate that, *in vitro*, mitochondrial activity is upregulated by oAß treatment, however, the magnitude of the activation was smaller than *in vivo* probably due to the rich medium used in culture. To investigate if a reduction of mitochondrial activity by an exacerbation of the HIF1 response could compromise microglial responses to Aß, we exposed

normoxic and hypoxic microglial cell primary cultures to oAß for 24 h. Interestingly, hypoxia reduced the basal levels of *Tnf* and *Il6* mRNA and blunted the normoxic response to oAß (Fig. 4c). A similar reduction in microglial response to the one observed in primary microglial cell cultures from *Trem2*$^{-/-}$ mice exposed to 3 h of oAß (Fig. 4c).

To further characterize the role of hypoxia in microglial cells, we first reanalyzed the transcriptomic data obtained from the primary microglial cells exposed to low oxygen levels (1% O_2, 6 h; Fig. 1d and Extended Data Fig. 1a). As expected, hypoxia induced a robust transcriptional response characterized by the coordinated induction of glycolytic genes (Fig. 4d, Extended Data Fig. 4a, and Supplementary Table 10). Correspondingly, the glycolytic rate showed a clear increase in primary microglial cells exposed to hypoxia (Fig. 4e). In parallel, low oxygen levels repressed mitochondrial oxidative phosphorylation, as shown by GSEA and oxygen consumption recordings in hypoxic primary microglial cultures (Fig. 4f–g, Extended Data Fig. 4b, and Supplementary Table 10). Consequently, *in cellulo* hypoxia induced a significant decrease in the ratio between the mitochondrial oxygen consumption and the glycolytic proton efflux rates in microglia (Fig. 4h). Interestingly, the upregulation of anaerobic glycolysis (Fig. 4d, e and Extended Data Fig. 4c, d) was accompanied by a drastic downregulation of the overall cellular function, including DNA replication, which suggests that slowdown of mitochondrial activity may induce microglial quiescence (Extended Data Fig. 5a, b).

To evaluate if hypoxia inhibited proliferation of microglia, we used two models: the microglial-derived BV2 cell line and mouse primary microglial cell cultures. To determine if hypoxia (1% O_2, 4 to 48 h) modulates BV2 cell cycle, we measured the percentage of cells in G0/G1, S, or G2 using propidium iodide (PI) staining and flow cytometry. Brief hypoxia (4 h) did not change the BV2 cell cycle; however, 24 and 48 h of hypoxia led to a dramatic cell cycle arrest (Extended Data Fig. 6a). To differentiate between the induction by hypoxia of senescence (irreversible cell cycle arrest) or quiescence (reversible), we exposed BV2 hypoxic cultures to 24 h of reoxygenation. Interestingly, cell cycle was completely restored after incubation in normoxia (Extended Data Fig. 6b). In order to evaluate the involvement of HIF in the control of cell cycle under hypoxia, we interfered the expression of *Hif1a*, *Epas1* (encoding for HIF2α) or *Hif1a* and *Epas1*. Although the degree of suppression reached was small (around 50 – 60% of the levels of non-interfered cultures; Extended Data Fig. 6c), we were able to observe a

decrease in the hypoxia-induced cell cycle arrest when both genes were knocked down (Extended Data Fig. 6c). To confirm the role of HIF in the hypoxia-mediated cell cycle arrest, we first exposed BV2 cells to dimethyloxalylglycine (DMOG), an inhibitor of the main negative regulators of HIF stability, the prolyl-hydroxylases (PHDs)[18], and observed a hypoxia-like cell cycle arrest in BV2 (Extended Data Fig. 6d). Second, we performed primary microglial cell cultures from either Egl9 homologue 2 (*Egln2*$^{-/-}$) (encoding for PHD1), *Egln1*$^{+/-}$ (PHD2, full PHD2 deficiency is not viable), or *Egln3*$^{-/-}$ (PHD3) mice. The number of microglial cells was decreased both in the absence of PHD3 or in the presence of half dose of PHD2 (Fig. 4i), whereas no differences were observed in PHD1-deficient microglia (Fig. 4i), further supporting a role for HIF in microglial proliferation[36,37]. Finally, we estimated proliferation in primary microglial cell cultures exposed to 24 h of hypoxia (1% O_2), using a bromodeoxyuridine (BrdU) incorporation assay. Hypoxia induced a notable decrease in BrdU reactive microglial cells (Fig. 4j). To confirm the role of HIF1 in the microglial cell cycle arrest induced by hypoxia, we used primary microglial cell cultures with conditional deletion of *Hif1a* (Fig. 1e) exposed to hypoxia. As expected, hypoxia produced a ~ 60% decrease in the number of BrdU-reactive cells. However, microglial proliferation was almost completely restored in HIF1α-deficient cultures (Fig. 4k), demonstrating that HIF1 contributes to the reversible microglial cell cycle arrest under hypoxia.

A decrease of mitochondrial metabolism *via* HIF1 reduces AßAM

The formation of new Aß plaques in APP overexpressing mouse models is associated with microglia proliferation[17,38]. However, we have shown that *in cellulo*, HIF1 overactivation induces microglial quiescence characterized by low response to oAß and a reversible cell cycle arrest (Fig. 4). Therefore, we postulated that the proliferation, and therefore the clustering, of microglia around Aß plaques *in vivo* depends on the balance between glycolysis and aerobic respiration.

In normoxia, *Hif* genes are constitutively transcribed and translated but the resultant protein is degraded by the proteasome through oxygen-dependent hydroxylation by PHDs and von Hippel-Lindau (VHL)-mediated ubiquitination[18]. As overstabilization of HIF1 by VHL deficiency induces anaerobic glycolysis and inhibition of aerobic respiration[39], we created a new conditional AD mouse model with VHL depletion in adult microglia (*Cx3cr1-Cre::ERT2/+*; *Vhl* $^{Flox/-}$; *APP-PSEN1/+*) (Fig. 5a). VHL deficiency induced the HMM *in vivo*, as demonstrated by

global expression profile studies in isolated microglia (Fig. 5b and Supplementary Table 11) and a decrease in the OXPHOS GS transcription (Fig. 5c). Interestingly, this transcriptional regulation was associated with a decrease in the percentage of microglia, as observed by flow cytometry (Fig. 5d). Remarkable, VHL-deficiency induced a decrease in the common microglial transcriptional phenotype (MGnD GS; Fig. 5e) in a transcriptional phenotype similar to TREM2 deficiency (for a review see[40]) that suggested reduced AßAM. Therefore, we quantified the IBA1 immunoreactivity around Aß plaques and observed a decrease in the microglial coverage of cortical Aß deposits in the absence of VHL (Fig. 5f). Altogether, these results indicate that the downregulation of AßAM aerobic respiration by HIF1 stabilization induces a microglial dysfunctional phenotype similar to the one observed in TREM2 deficiency.

Several modifiable AD risk factors (e.g. hypertension, obesity, atrial fibrillation, diabetes, physical inactivity, and smoking) converge in altering the vascular system and/or reducing oxygen/nutrient availability[20,22]. We reasoned that those AD risk factors could contribute to the microglial dysfunction described in the human AD brain by disrupting the HIF1/aerobic respiration metabolic equilibrium observed in AßAM. To test that idea, we exposed 14-month-old WT or *APP-PSEN1/+* mice to either normoxia (21% O_2) or sustained hypoxia (9% O_2) for 21 days and quantified IBA1+ microglia in the hippocampus. We found a significant decrease in the number of IBA1+ microglia in hypoxic *APP-PSEN1/+* mice compared to normoxic *APP-PSEN1/+* mice, whereas only a trend was detected in hypoxic compared to normoxic WT mice (Fig. 6a). Similarly, qRT-PCR in hippocampal extracts rendered significantly reduced levels of *Iba1* mRNA without changing the *glial fibrillary acidic protein* (*Gfap*) astrocytic mRNA levels in *APP-PSEN1/+* (Fig. 6b) and no differences were found in WT mice (Extended Data Fig. 7a). More strikingly, the distribution of microglia was altered by sustained hypoxia, showing absence of clustering around Aß plaques (Fig. 6a), suggesting a defect in AßAM. A closer examination of hippocampal and cortical regions of *APP-PSEN1/+* mice revealed that hypoxic AßAM did not invade the plaques or were simply absent (Fig. 6c), a phenocopy of the microglial dysfunction observed in microglia deficient for VHL (Fig. 5f) and in TREM2 deficient mice[40]. This observation was confirmed using tomato lectin (TL) as an independent microglial marker (Fig. 6c). Quantification of both the $IBA1^+$ cell number and the area occupied by $IBA1^+$ staining per Thio-S+ plaque demonstrated fewer AßAM in the hippocampus and the cortex of hypoxic

versus normoxic *APP-PSEN1/+* mice (Fig. 6d). In sharp contrast, neither the number of reactive astrocytes ($GFAP^+$) nor the number of total astrocytes (glutamine synthetase, $GluS^+$) was altered by sustained hypoxic treatment in *APP-PSEN1/+* mice (Extended Data Fig. 7b). Moreover, the ratio of astrocytes adjacent to Aß plaques (within 20 µm from the plaque edge) *versus* total astrocytes was not significantly different (Extended Data Fig. 7b, c). The sustained hypoxia treatment induced an expected increase in hematocrit (Extended Data Fig. 7d) and no infarctions were observed in the hypoxic brains of WT or *APP-PSEN1/+* mice (Extended Data Fig. 7e). Finally, we showed that hypoxia reduced AßAM proliferation using Ki67 staining in the hippocampus and in the cortex of *APP-PSEN1* mice (Fig. 6e) and no changes were observed by hypoxic treatment in WT mice (Extended Data Fig. 7f).

Altogether, these results suggest that systemic comorbidities may contribute to brain hypoxia/hypoperfusion-induced microglial quiescence by disrupting the HIF1/aerobic respiration metabolic equilibrium in AßAM.

Sustained hypoxia enhances Aß local pathology

Defects in microglial clustering around plaques by *TREM2* haplo-insufficiency decreased Aß plaque compaction[9,10], highlighting the protective barrier function of microglia around plaques[3]. We therefore asked whether the reduced clustering of microglia induced by sustained hypoxia correlated with an increase in Aß levels in *APP-PSEN1/+* mice. We observed a significant increase in both dense-core Thio-S^+ and total Aß+ plaque load and number in the cortex of hypoxic *APP-PSEN1/+* mice (9% O_2) compared to normoxic (21% O_2) AD littermates (Fig. 7a–f), despite no significant differences in the total Aß levels by ELISA nor in the processing of APP[41]. As a control, we also show that no Thio-S^+ (Extended Data Fig. 8a) or $Aß^+$ (Extended Data Fig. 8b) plaques were found in normoxic or hypoxic WT mice. Furthermore, the size distribution of cortical Thio-S^+ and total $Aß^+$ plaques in hypoxic and normoxic *APP-PSEN1/+* mice revealed an enrichment in plaques under hypoxia, suggesting that low oxygen enhances Aß aggregation resulting in more newly-formed plaques (Fig. 7c, f). Levels of soluble $Aß_{1-42}$ in normoxic and hypoxic *APP-PSEN1/+* mice measured by ELISA showed a trend to increase under hypoxia (Fig. 7g) and dot blots with a fibrillar Aß oligomers-specific antibody (OC) showed a clear increase of OC immunoreactivity in cortical soluble extracts from hypoxic *versus*

normoxic *APP-PSEN1/+* mice (Fig. 7h). Altogether, these data suggest that sustained hypoxia potentiates Aß aggregation and deposition in the brain parenchyma.

As the result of the direct neurotoxic effect of Aß, dense-core (senile) plaques are decorated with dystrophic neurites, which can be displayed with both ubiquitin (UB) and phospho-TAU (p-TAU) immunohistochemistry. The AD-linked p.R47H and p.R62H TREM2 variants impair the microglia barrier function and worsens plaque-associated axonal dystrophies[9–11]. Therefore, we investigated whether sustained hypoxia could aggravate this neurodegenerative feature in an AD mouse model. *APP-PSEN1/+* mice exposed to sustained hypoxia showed a trend to increase in the UB load (Fig. 7i) and a clear augmentation in the density of p-TAU$^+$ dystrophic neurites per Thio-S$^+$ plaque (Fig. 7j). As expected, we also show that no p-TAU$^+$ dystrophic neurites (Extended Data Fig. 8c) were found in normoxic or hypoxic WT mice. We have previously shown that hippocampal somatostatin and neuropeptide Y interneurons are particularly vulnerable and die at early stages in a similar AD mouse model[42]. Here, we detected a significant further decrease in the mRNA levels of both somatostatin (*Sst*) and neuropeptide Y (*Npy*) under sustained hypoxic stress (Fig. 7k). Thus, these data indicate that sustained hypoxia leads to an increase in soluble Aß fibrillar oligomers and newly formed dense-core Aß plaques, and aggravates Aß plaque-associated neurodegenerative phenomena.

Nude Aß plaques with high pathology in hypoxic brain areas

To study the contribution of HIF1 induction in the AD human brain, we first reanalysed the data of an RNAseq study of isolated cell types from the human brain[43]. Interestingly, *HIF1a* transcript was highly abundant in human microglia when compared with other cells types (Fig. 8a), suggesting a preponderant role of HIF1 in those cells. AD-associated microglial degeneration has mainly been observed in the human hippocampus[6,7]. To evaluate the potential contribution of HIF1 to AD, we measured the levels of *HIF1a* mRNA by qRT-PCR and HIF1α protein by Western blot in hippocampal samples from AD and non-demented control individuals (Supplementary Table 12). Both mRNA (a non-significant trend) and protein levels were upregulated, paralleling the progression of AD pathology (Fig. 8b). The drop in HIF1α levels at advanced (Braak V-VI) compared with intermediate (Braak III-IV) stages is likely explained by the dramatic end-stage cell death and atrophy. We also demonstrated the up-regulation of the mRNA levels of several HIF-regulated genes in AD (Braak V-VI) human hippocampal samples

(Fig. 8c), suggesting that advances stages of the pathology are associated with induction of HIF1.

Human microglial pathology is mainly concentrated in the hilar region of the dentate gyrus[7], a brain area with relatively low oxygen levels to preserve neurogenesis[44]. To investigate the contribution of hypoxia to microglial degeneration, we compared Aß plaques from the dentate gyrus (hypoxia-prone region) with those from the perirhinal cortex (control region), as both brain areas accumulate similar large diffuse neuritic plaques[45]. Remarkably, a significant microglial depopulation of senile plaques was observed at Braak V-VI stages at the molecular layer of the dentate gyrus, when compared with plaques from the perirhinal cortex of the same individuals (Fig. 8d), suggesting that local hypoxia also primes AßAM dysfunction in the human AD brain, generating nude Aß plaques.

An increase in plaque-associated axonal dystrophies have been observed in the brain of carriers of the AD-linked TREM2 variants[9,10] and sustained hypoxia incremented the local neuropathology in an AD mouse model (Fig. 7i, j). Therefore, we investigated if the nude Aß plaques in the human dentate gyrus were also enriched in dystrophic neurites. Triple combined immunohistochemistry for p-TAU, IBA1, and Aß in Braak V–VI hippocampal samples revealed plaques presented dystrophic neurites in the zones of the plaques that were devoid of microglia (Fig. 8e). To quantitatively demonstrate the relation between nude Aß plaques and increased local pathology, we measured the area occupied by IBA1 (microglia), AT8 (p-TAU), and Aß per plaque. We anticipate that a microglial area lower than the Aß area (protection index < 1, measured per individual plaque) should be less protected than Aß plaques with larger microglial occupancy (protection index > 1) for the formation of AT8 reactive dystrophies. In fact, we demonstrated that Aß plaques with a protection index smaller than 1 presented higher dystrophic neurites (Fig. 8e). As a control, we also checked that both groups (protection index < 1 and > 1) had similar Aß plaque size distribution (Fig. 8e).

Altogether, our data strongly suggest that, similar to what was found in TREM2 risk allele carriers[9,10], nude Aß plaques associate with hypoxia-prone human brain areas and elevated local neuronal pathology in AD patients.

DISCUSSION

Increasing evidence indicates that the microglial defensive activity is required to halt the progression of AD[3,5,9–11]. At the same time, microglia are the cells able to survive closer to Aß deposits[17]. Therefore, to understand how these cells survive and provide a full response under challenging conditions is of utmost importance. We show here that AßAM is characterized by the paradoxical concomitant activation of HIF1-induced anaerobic glycolysis and the aerobic respiration, suggesting local metabolic stress around Aß plaques. We also show that sustained overactivation of HIF1 induces microglial quiescence *in cellulo* and a decrease in the ability of AßAM to proliferate and cluster around Aß plaques *in vivo*. HIF1-mediated reduced coverage of Aß plaques associates with worsening of AD neuropathology both in AD mouse models and in the human AD brain, highlighting the relevance of modifiable AD risk factors related with HIF1 activation.

From its discovery, microglial cells were characterized by a surprising morphological plasticity[1], which is also observed around Aß plaques, where microglia proliferate, migrate and emit thick cytoplasmic projections that constitute a physical barrier against Aß spreading[3,9,10]. These morphologic adaptations are accompanied with an exuberant transcriptional modulation that optimize AßAM responses[13,25,26]. Between those transcriptional responses, we found that the aerobic respiration is highly enriched in DAM transcription. In innate immune cells, HIF1 activation is normally associated with a metabolic switch from aerobic respiration to anaerobic glycolysis, and the activation of a pro-inflammatory program that include cytokine production through increased inflammasome signaling[18,46]. It have been suggested that, in AD microglia, TREM2 activation could reduce this acute response to sustain long-term activity[16]. In the light of our results, TREM2 activation entails an aerobic respiration-based metabolism, which may counteract a switch towards a pro-inflammatory state of DAM. In AßAM, however, this equilibrium is at risk, as basal activity of HIF1 is detected and mitochondria elongate, a characteristic response of cells that maintain aerobic respiration under low oxygen and nutrient stress[34]. Mitochondrial elongation maximizes tricarboxylic acid cycle (TCA) functioning for biosynthesis and ATP production, sustaining cell viability under oxygen and nutrient deprivation and prevents hypoxia- and/or low nutrients-induced mitophagy[35]. TREM2 activation of mTOR has been shown as pivotal for the microglial metabolic adaptation to confront Aß deposition[16,19],

and the mitochondrial metabolism may be regulated by mTOR through increased translation of the transcription factor A, mitochondrial (TFAM) and other key factors[32]. However, the mTOR-mediated anabolic induction is reduced when nutrient (including oxygen) supply is inadequate *via* increased HIF1 transcription and translation. Further work will be required to demonstrate the role of the TREM2/mTOR pathway in regulation of mitochondrial AßAM metabolism.

The severe AßAM dependence on mitochondrial oxidative phosphorylation was revealed by forcing the inhibition of microglial mitochondrial activity *via* (i) sustained hypoxia *in cellulo*, which induces a slowdown in microglial proliferation and quiescence, or, *in vivo*, by (ii) VHL deficiency or (iii) sustained hypoxia, mimicking AD modifiable risk factors that reduce brain perfusion/oxygenation (e.g. hypertension, obesity, atrial fibrillation, diabetes mellitus, physical inactivity, smoking[20], and intracerebral atherosclerosis[47]). Similarly, overactivation of HIF1 in microglia by systemic LPS injection also resulted in a shift towards anaerobic glycolysis, production of proinflammatory cytokines, and worsening of AD neuropathology[19]. Inversely, both sodium rutin (a natural flavonoid that induces a switch from anaerobic glycolysis to aerobic respiration in microglia) and interferon gamma (an inductor of mTOR) attenuated neuroinflammation[48], enhanced AßAM clustering and phagocytosis[23,48], and ameliorated the learning and memory defects observed in amyloidogenic models[23,48]. Interestingly, age, the main risk factor for AD[20], may induce a decrease in the mouse microglial OXPHOS GS (Extended Data Fig. 3c), suggesting that age could also merge with AD genetic[14–16,26] and modifiable risk factors in hijacking microglial aerobic respiration. The relation between aging and microglial mitochondrial function will require additional experimental work.

The reduced AßAM proliferation and clustering by HIF1 overactivation resembles the phenotype observed in (i) the brain of *TREM2* p.R47H and p.R62H carriers and in AD mouse models with either (ii) genetic *Trem2* deficiency or (iii) expressing these AD-linked loss of function[9,10], and also resulted in increased neuropathology. Thus, in addition to other factors[22], systemic sustained hypoxia contributes to AD progression by decreasing the microglial ability to proliferate and confine Aß deposits. Therefore, both genetic (TREM2/APOE), systemic (infections or brain hypoperfusion/hypoxia), and local stress (HIF1) factors converge in reducing AD microglial clustering and, therefore, their barrier function[5]. Correspondingly, a recent study has highlighted the role of brain atherosclerosis in AD, suggesting a direct molecular link[47,49].

Of note, we also demonstrated that the human AD brain accumulates HIF1 and HIF1 targets, that a hypoxia-prone region is characterized by the presence of “nude” (microglia-free) Aß plaques, and that the absence of microglia correlates with increased periplaque p-TAU dystrophic neurites. Notably, recent epidemiologic studies have estimated that between a third and a half of AD cases could be attributable to modifiable risk factors[50–52] and have suggested that, as age-adjusted incidence and prevalence of dementia might be decreasing (reviewed in[21]), AD may be preventable. Our results also pave the way for the search of pharmacologic agents that could improve the mitochondrial metabolic fitness of microglia against the stress imposed by Aß plaques and, likely, reduce the progression of AD.

1. Río-Hortega, P. El “tercer elemento” de los centros nerviosos. I. La microglía en estado normal. II. Intervención de la microglía en los procesos patológicos (células en bastoncito y cuerpos gránulo-adiposos). *Bol. Soc. Esp. Biol.* **VIII**, 69–103 (1919).
2. Sierra, A. *et al.* The “Big-Bang” for modern glial biology: Translation and comments on Pío del Río-Hortega 1919 series of papers on microglia. *Glia* **64**, 1801–1840 (2016).
3. Condello, C., Yuan, P., Schain, A. & Grutzendler, J. Microglia constitute a barrier that prevents neurotoxic protofibrillar Aβ42 hotspots around plaques. *Nat. Commun.* **6**, 6176 (2015).
4. Bertram, L. & Tanzi, R. E. Alzheimer disease risk genes: 29 and counting. *Nat. Rev. Neurol.* **15**, 191–192 (2019).
5. Colonna, M. & Wang, Y. TREM2 variants: new keys to decipher Alzheimer disease pathogenesis. *Nat. Rev. Neurosci.* **17**, 201–207 (2016).
6. Streit, W. J., Xue, Q. S., Tischer, J. & Bechmann, I. Microglial pathology. *Acta Neuropathol. Commun.* **2**, 1–17 (2014).
7. Sanchez-Mejias, E. *et al.* Soluble phospho-tau from Alzheimer’s disease hippocampus drives microglial degeneration. *Acta Neuropathol.* **132**, 897–916 (2016).
8. Lassmann, H. *et al.* Cell death in Alzheimer’s disease evaluated by DNA fragmentation in situ. *Acta Neuropathol.* **89**, 35–41 (1995).
9. Yuan, P. *et al.* TREM2 Haplodeficiency in Mice and Humans Impairs the Microglia Barrier Function Leading to Decreased Amyloid Compaction and Severe Axonal Dystrophy. *Neuron* **90**, 724–739 (2016).
10. Leyns, C. E. G. *et al.* TREM2 function impedes tau seeding in neuritic plaques. *Nat. Neurosci.* (2019). doi:10.1038/s41593-019-0433-0
11. Wang, Y. *et al.* TREM2-mediated early microglial response limits diffusion and toxicity of amyloid plaques. *J. Exp. Med.* **213**, 667–675 (2016).
12. Lucin, K. M. & Wyss-Coray, T. Immune Activation in Brain Aging and Neurodegeneration: Too Much or Too Little? *Neuron* **64**, 110–122 (2009).
13. Holtman, I. R. *et al.* Induction of a common microglia gene expression signature by aging and neurodegenerative conditions: a co-expression meta-analysis. *Acta Neuropathol. Commun.* **3**, 31 (2015).

14. Sala Frigerio, C. *et al.* The Major Risk Factors for Alzheimer's Disease: Age, Sex, and Genes Modulate the Microglia Response to Aβ Plaques. *Cell Rep.* **27**, 1293-1306.e6 (2019).

15. Ulrich, J. D. *et al.* ApoE facilitates the microglial response to amyloid plaque pathology. *J. Exp. Med.* 1–17 (2018). doi:10.1084/jem.20171265

16. Ulland, T. K. *et al.* TREM2 Maintains Microglial Metabolic Fitness in Alzheimer's Disease. *Cell* **170**, 649-663.e13 (2017).

17. Serrano-Pozo, A. *et al.* Differential Relationships of Reactive Astrocytes and Microglia to Fibrillar Amyloid Deposits in Alzheimer Disease. *J. Neuropathol. Exp. Neurol.* **72**, 462–471 (2013).

18. Kaelin, W. G. & Ratcliffe, P. J. Oxygen Sensing by Metazoans: The Central Role of the HIF Hydroxylase Pathway. *Mol. Cell* **30**, 393–402 (2008).

19. Wendeln, A.-C. *et al.* Innate immune memory in the brain shapes neurological disease hallmarks. *Nature* **556**, 332–338 (2018).

20. Livingston, G. *et al.* Dementia prevention, intervention, and care. *Lancet* **390**, 2673–2734 (2017).

21. Serrano-Pozo, A. & Growdon, J. H. Is Alzheimer's Disease Risk Modifiable? *J. Alzheimer's Dis.* **67**, 795–819 (2019).

22. Zlokovic, B. V. Neurovascular pathways to neurodegeneration in Alzheimer's disease and other disorders. *Nat. Rev. Neurosci.* **12**, 723–738 (2011).

23. Baik, S. H. *et al.* A Breakdown in Metabolic Reprogramming Causes Microglia Dysfunction in Alzheimer's Disease. *Cell Metab.* 1–15 (2019). doi:10.1016/j.cmet.2019.06.005

24. Puente-Santamaria, L., Wasserman, W. W. & Del Peso, L. TFEA.ChIP: A tool kit for transcription factor binding site enrichment analysis capitalizing on ChIP-seq datasets. *Bioinformatics* **35**, 5339–5340 (2019).

25. Keren-Shaul, H. *et al.* A Unique Microglia Type Associated with Restricting Development of Alzheimer's Disease. *Cell* **169**, 1–15 (2017).

26. Krasemann, S. *et al.* The TREM2-APOE Pathway Drives the Transcriptional Phenotype of Dysfunctional Microglia in Neurodegenerative Diseases. *Immunity* **47**, 566-581.e9

(2017).

27. Chiu, I. M. *et al.* A neurodegeneration-specific gene-expression signature of acutely isolated microglia from an amyotrophic lateral sclerosis mouse model. *Cell Rep.* **4**, 385–401 (2013).

28. Hickman, S. E. *et al.* The microglial sensome revealed by direct RNA sequencing. *Nat. Neurosci.* **16**, 1896–905 (2013).

29. Wang, Y. *et al.* TREM2 lipid sensing sustains the microglial response in an Alzheimer's disease model. *Cell* **160**, 1061–71 (2015).

30. Grubman, A. *et al.* A single-cell atlas of entorhinal cortex from individuals with Alzheimer's disease reveals cell-type-specific gene expression regulation. *Nat. Neurosci.* **22**, (2019).

31. Morita, M. *et al.* MTORC1 controls mitochondrial activity and biogenesis through 4E-BP-dependent translational regulation. *Cell Metab.* **18**, 698–711 (2013).

32. Morita, M. *et al.* mTOR coordinates protein synthesis, mitochondrial activity and proliferation. *Cell Cycle* **14**, 473–480 (2015).

33. Steinman, J., Sun, H.-S. & Feng, Z.-P. Microvascular Alterations in Alzheimer's Disease. *Front. Cell. Neurosci.* **14**, (2021).

34. Li, J. *et al.* Mitochondrial elongation-mediated glucose metabolism reprogramming is essential for tumour cell survival during energy stress. *Oncogene* **36**, 4901–4912 (2017).

35. Gomes, L. C. & Scorrano, L. Mitochondrial elongation during autophagy. *Autophagy* **7**, 1251–1253 (2011).

36. Ginouvès, A., Ilc, K., Macías, N., Pouysségur, J. & Berra, E. PHDs overactivation during chronic hypoxia 'desensitizes' HIFalpha and protects cells from necrosis. *Proc. Natl. Acad. Sci. U. S. A.* **105**, 4745–4750 (2008).

37. Berra, E. *et al.* HIF prolyl-hydroxylase 2 is the key oxygen sensor setting low steady-state levels of HIF-1alpha in normoxia. *EMBO J.* **22**, 4082–4090 (2003).

38. Bondolfi, L. *et al.* Amyloid-associated neuron loss and gliogenesis in the neocortex of amyloid precursor protein transgenic mice. *J. Neurosci.* **22**, 515–522 (2002).

39. Papandreou, I., Cairns, R. A., Fontana, L., Lim, A. L. & Denko, N. C. HIF-1 mediates adaptation to hypoxia by actively downregulating mitochondrial oxygen consumption.

Cell Metab. **3**, 187–197 (2006).

40. Zhou, Y., Ulland, T. K. & Colonna, M. TREM2-dependent effects on microglia in Alzheimer's Disease. *Front. Aging Neurosci.* **10**, 1–7 (2018).

41. Serrano-Pozo, A. *et al.* Acute and Chronic Sustained Hypoxia Do Not Substantially Regulate Amyloid-β Peptide Generation In Vivo. *PLoS One* **12**, e0170345 (2017).

42. Ramos, B. *et al.* Early neuropathology of somatostatin/NPY GABAergic cells in the hippocampus of a PS1xAPP transgenic model of Alzheimer's disease. *Neurobiol. Aging* **27**, 1658–1672 (2006).

43. Zhang, Y. *et al.* Purification and Characterization of Progenitor and Mature Human Astrocytes Reveals Transcriptional and Functional Differences with Mouse. *Neuron* **89**, 37–53 (2016).

44. Chatzi, C., Schnell, E. & Westbrook, G. L. Localized hypoxia within the subgranular zone determines the early survival of newborn hippocampal granule cells. *Elife* **4**, 1–18 (2015).

45. Thal, D. R. *et al.* Sequence of Aβ-Protein Deposition in the Human Medial Temporal Lobe. *J. Neuropathol. Exp. Neurol.* **59**, 733–748 (2000).

46. Weichhart, T., Hengstschläger, M. & Linke, M. Regulation of innate immune cell function by mTOR. *Nat. Rev. Immunol.* **15**, 599–614 (2015).

47. Wingo, A. P. *et al.* Shared proteomic effects of cerebral atherosclerosis and Alzheimer's disease on the human brain. *Nat. Neurosci.* **23**, 1–5 (2020).

48. Pan, R.-Y. *et al.* Sodium rutin ameliorates Alzheimer's disease–like pathology by enhancing microglial amyloid-β clearance. *Sci. Adv.* **5**, eaau6328 (2019).

49. Iadecola, C. Revisiting atherosclerosis and dementia. *Nat. Neurosci.* **23**, 41–42 (2020).

50. Ashby-Mitchell, K., Burns, R., Shaw, J. & Anstey, K. J. Proportion of dementia in Australia explained by common modifiable risk factors. *Alzheimer's Res. Ther.* **9**, 1–8 (2017).

51. Norton, S., Matthews, F. E., Barnes, D. E., Yaffe, K. & Brayne, C. Potential for primary prevention of Alzheimer's disease: An analysis of population-based data. *Lancet Neurol.* **13**, 788–794 (2014).

52. Barnes, D. E. & Yaffe, K. The projected effect of risk factor reduction on Alzheimer's

disease prevalence. *Lancet Neurol.* **10**, 819–828 (2011).

53. Herzenberg, L. a, Tung, J., Moore, W. a, Herzenberg, L. a & Parks, D. R. Interpreting flow cytometry data: a guide for the perplexed. *Nat. Immunol.* **7**, 681–5 (2006).

Acknowledgments

We thank Prof. Sir Peter J. Ratcliffe for hosting A.H.-G. in his laboratory for PHDs experiments and Dr. Luis del Peso for his assistance with the TFEA use. We also wish to thank K. Levitsky (microscopy), M.J. Castro (flow cytometry), F.J. Moron (genomics), and R. Duran (histology) for advice and technical assistance in experiments at IBiS core facilities. R.M.-D. was the recipient of a “Sara Borrell” fellowship from ISCIII (CD09/0007), N.L.-U., C.O-dSL., C. R.-M., and M.I.A.-V. were the recipient of an FPU fellowship from Spanish Ministry of Education, Culture, and Sport (respectively, FPU14/02115, AP2010-1598, FPU16/02050, and FPU15/02898), A.H.-G. was the recipient of an FPI fellowship from Spanish Ministry of Education, Culture, and Sport (BES-2010-033886). Work was supported by grants to A.P. by the Spanish MINEICO, ISCIII, and FEDER (EU) (SAF2012-33816, SAF2015-64111-R, SAF2017-90794-REDT, and PIE13/0004), by the regional Government of Andalusia (“Proyectos de Excelencia", P12-CTS-2138 and P12-CTS-2232) co-funded by CEC and FEDER funds (EU), and by the "Ayuda de Biomedicina 2018", Fundación Domingo Martínez; to AG and JV: Instituto de Salud Carlos III (ISCiii) of Spain, co-financed by FEDER funds (EU), through grants PI18/01556 (JV) and PI18/01557 (AG), and by Junta de Andalucia co-financed by FEDER funds: grants UMA18-FEDERJA-211 (AG) and US-1262734 (JV); and to EB: Spanish MINEICO (BFU2016-76872-R and BES-2011-047721).

Author Contributions Statement

A. P., J. V., R. M.-D., N. L.-U., C. R.-M., A. H.-G., and C. O.-S.L., conceived and designed research; A. P., R. M.-D., N. L.-U., C. R.-M., A. H.-G., M. I. A.-V., M. A. S.-G., E. S.-M., J. C. D., A. E. R.-N., V. N., A. G.-A., M. V. S.-M., A. V., and A. G., performed research; A. P., R. M.-D., N. L.-U., C. R.-M., A. H.-G., M. I. A.-V., M. A. S.-G., E. S.-M., J. C. D., A. E. R.-N., C. F., V. N., A. G.-A., M. V. S.-M., A. V., A. G., M. V., T. B., A. S.-P., J. L.-B., E. B., J. V., and A. P., analyzed the data; E. J. H., and T. B., provided methodological and/or scientific assistance; E. J. H., and T. B. contributed with mouse models/samples; A. P, E. B., J. V., and A. S.-P., wrote the manuscript.

Competing Interests Statements

The authors declare no competing interests.

FIGURE LEGENDS

Fig. 1 | HIF1-mediated transcription is activated in AßAM. a, **b**, ISH of *Hif1a* mRNA (brown) and immunohistochemistry for microglia (IBA1, green), nuclear (DAPI; blue) staining in brain sections of 8-month-old *APP-PSEN1/+* mice proximal (**a**) and distal (**a**, **b**) to Aß plaques (yellow asterisks in **a**). Red arrowheads indicate microglia proximal to Aß plaques and yellow arrowheads depict microglial cells not associated with Aß. Right in (**b**), microglial quantification of $IBA1^{+}/Hif1a^{+}$ cells in WT and in distal and proximal regions to Aß plaques (n = 4 mice; ANOVA, post hoc Tukey's test). **c**, Transcription Factor Enrichment Analysis (TFEA) of *APP-PSEN1/+* microglial transcription[24]. Each dot in the volcano plot represents an individual CHIP-seq experiment. **d**, Volcano plot (right panel) showing the genes included in the hypoxia/HIF1-induced microglial module (HMM) (red dots; $p < 0.01$, LogFC > 0.5). **e**, Primary microglial cell cultures from *Cx3cr1-Cre::ERT2/+*; *Hif1a* $^{Flox/Flox}$ mice either treated with vehicle (C) or tamoxifen (T; 100 nM; 6 d) and the effect on HIF1α expression assayed by qRT-PCR (left panel; n = 7; Student's t-test) and by western (right panel) in normoxia (N: 21% O_2, 24 h) and after DMOG (D: 0.1 mM, 24 h) treatment. **f**, Primary microglial cell cultures from *Cx3cr1-Cre::ERT2/+*; *Hif1a* $^{Flox/Flox}$ mice treated either with vehicle, D, T, or D and T, and the mRNA fold change in D *versus* vehicle (D) and D and T *versus* T are represented. *Hmbs* levels used as housekeeping controls (n = 5 *Vegfa, Ero1l, Prr15,* and *Mxi1*; 3 *Bhlhe40*; 6, *Ccng2*; and 4 *Egln1*; Student's t-test, two-sided). **g**, Gene set enrichment analysis (GSEA) of $APP_{751}SL/+$ DAM *versus* (*vs*) WT 12-month-old microglia. Heat maps showing top 30 ranking genes of the HMM (left) and MGnD (right) gene sets (GSs). Red symbolizes overexpression and blue down regulation (see Supplementary Data Table for shade values). Right table: 15 top GSs with FWER-p-value less than 0.05 are listed.

Data are presented in all the graphs as mean ± standard error of the mean (S.E.M.). n are biological independent experiments.

Fig. 2 | AD microglia increase aerobic respiration-related transcription. a, GSEA of $APP_{751}SL/+$ DAM *versus* (*vs*)) WT 12-month-old microglia. Heat maps of top 30 ranking leading edge genes of the oxidative phosphorylation (OXPHOS) GS. Red symbolizes overexpression and blue down regulation (see Supplementary Data Table for shade values). **b**, Aerobic respiration-related GSs enriched in $APP_{751}SL/+$ DAM *vs* WT microglia. **c**, Single-nuclei RNA

sequencing of human entorhinal cortex (http://adsn.ddnetbio.com/[30]). Upper row, left: UMAP visualization of microglial cells from AD and control samples. Upper row right and lower row: Relative gene expression (color intensity) of four representative OXPHOS genes. The table includes the changes in expression (Log_2 fold change and FDR *q*-values) of the OXPHOS genes between AD and control microglial cells. **d**, Enrichment plot and heat map of the OXPHOS GS in *Trem2*$^{-/-}$; *5xfAD/+ vs 5xfAD/+* microglia.

Fig. 3 | Mitochondria is elongated in an AD mouse model. a, Left panels, cortical confocal XY images from 8-month-old *APP-PSEN1/+* mice stained with mitochondrial complex I (NDUFS2; green), microglia (IBA1; red), and nuclear (DAPI; blue) markers. Arrows and arrow heads respectively indicate proximal and distal microglia. Right graph, quantification of the microglial (IBA1$^+$) NDUFS2 signal in WT mice and in distal and proximal areas to Aß plaques (*n* = 4 mice; ANOVA, post hoc Tukey's test). **b**, **c**, Electron microscopy images of hippocampal brain sections distal (**b**) and proximal (**c**) to Aß plaques in pathologic state *APP-PSEN1/+* mice. Microglia can be recognized by its darker cytoplasm and mitochondria by their morphology. Mitochondria are highlighted with yellow arrows. Some dystrophic neurites are labelled with pink circles as indicators of Aß proximity. c1, c2, and c4: Low magnification image of an Aß plaque. Blue arrowheads indicate microglial cells. c2, c3, and c5 are magnifications of the white rectangles. Please note that c3 panel has been rotated 90 degree from the original image (c2). **d**, Quantification of perimeter, aspect ratio, and circularity of mitochondria from microglial cells from WT and distal and proximal to Aß plaques (*n* is indicated between brackets; data from 4 WT and 3 *APP-PSEN1/+* mice; Mann-Whitney U's test with Post-hoc Dunn's test).

Data are presented in all the graphs as mean ± S.E.M. *n* are biological independent experiments.

Fig. 4 | Hypoxia induces cell-cycle arrest *via* HIF1 in microglia *in cellulo*. a, Mitochondrial respiration oxygen consumption rate (OCR; left) and maximal respiration (right) of control (C) or oligomeric Aß-treated (oAß; 10 µm; 24 h) mouse primary microglial cultures by Seahorse. Discontinued lines show injection (FCCP: carbonyl cyanide-4 (trifluoromethoxy) phenylhydrazone) (*n* = 3 independent cultures; Student's *t*-test). **b**, Protein levels of SDHA, NDUFS2, and ATPsynß in cultures treated as in (**a**). RPL26 was used as housekeeping (*n* is indicated between brackets; Student's *t*-test). **c**, *Tnf* and *Il6* mRNA levels in cultures treated as

in (**a**) and exposed to normoxia (N; 21% O_2; 24 h) or Hypoxia (H; 1% O_2; 24 h) (upper row) or from WT or *Trem2*$^{-/-}$ mice (lower row) (*n* is indicated between brackets; Student's *t*-test). **d**, **f**, Heat map of mouse primary microglial cultures in H (6 h) *versus* N. The top 30 ranking genes shown; red symbolizes overexpression and blue downregulation (see Supplementary Data Table for shade values). **e**, Extracellular acidification rate (left) and basal proton efflux rate (right) of mouse primary microglial cultures in N or H (24 h) by Seahorse. 2-DG, 2-deoxyglucose (*n* = 5 N and 6 H; Student's *t*-test). **g**, Mitochondrial respiration OCR (left) and basal respiration OCR (right) of mouse primary microglial cultures in normoxia (N) or H (24 h) by Seahorse. Discontinued lines show injection (*n* = 5 cultures in N and 6 in H: Student's *t*-test). **h**, Mitochondrial respiration OCR (mytoOCR)-basal proton efflux rate (glycoPER) ratio of mouse primary microglial cultures in N or H by Seahorse (*n* = 4 N and 6 H; Student's *t*-test). **i**, Left: images of primary microglial cultures stained with IBA1 (red) and GFAP (green), and counterstained with DAPI (blue) from WT (*Egln1*$^{+/+}$) or *Egln1*$^{+/-}$ mice. Right graphs show percentage of microglia in each mutant (KO or HET) relative to their control (C). (*n* is indicated between brackets; Student's *t*-test). **j**, Images of proliferation in primary microglial cultures (red) in either N, H, or DMOG (D, 24 h, 0.1 mM), and incubated with 10 µM bromodeoxyuridine (BrdU; 3h). Insets show a magnification of dotted squares. White arrowheads: BrdU^{+}/IBA1^{-}; green arrowhead: BrdU^{+}/IBA1^{-}. The quantification shown in the right graph (*n* = 4; Student's *t*-test). **k**, Primary microglial cultures from *Cx3cr1-Cre::ERT2-Hif* $^{Flox/Flox}$ mice treated either with vehicle (C) or tamoxifen (T; 100 nM, 6 d) and the number of BrdU reactive microglial cells in H (24 h) was estimated and presented as the percentage of N (*n* = 7 C, 6 T; Student's *t*-test).

Data are presented in all the graphs as mean ± S.E.M. Student's *t*-tests were two-sided. *n* are biological independent experiments.

Fig. 5 | Overstabilization of HIF1 reduces AßAM *in vivo*. Analysis of microglia from *Cx3cr1-Cre::ERT2*/+ *APP-PSEN1*/+; *Vhl*$^{Flox/-}$ mice non-treated (Control) or treated (VHL–) with tamoxifen (TMX, 30 days). **a**, Schematic representation of the mouse models used to generate genetic hypoxia (HIF overstabilization by VHL deletion) in adult microglia. **b, c**, GSEA. Heat maps and enplots of up to the top 30 ranking leading edge genes and enrichment plot of HMM (**b**) and OXPHOS (**c**) GSs. Red symbolizes overexpression and blue down regulation (see Supplementary Data Table for shade values). **d**, Adult microglia were isolated from control or

696 treated (VHL–) with tamoxifen (30 d) mice, using fluorescence-activated cell sorting (left graph).
697 Right graph, quantification of the percentage of $CD45^+/CD11b^+$ cells in mice without (C) or with
698 tamoxifen (VHL–) treatment (*n* = 5; Student's *t*-test, two-sided). **e**, Heat map and enrichment
699 plot of the MGnD GS. **f**, Left panels, cortical sections stained with IBA1 (red) and Thioflavin-S
700 (Thio-S; green). Scale bars are 20 µm. Right graph, quantification of the percentage of Aß
701 plaque area occupied by IBA1+ microglia in in mice treated without (C; pale pink bar) or with
702 tamoxifen (VHL–; 30 d; green bar) (*n* is indicated between brackets; Student's *t*-test, two-sided).
703 Data are presented in all the graphs as mean ± S.E.M. *n* are biological independent
704 experiments.
705 **Fig. 6 | Systemic sustained hypoxia decreases clustering of AßAM. a–e**, 14-month-old WT
706 and *APP-PSEN1/+* (AD) mice in normoxia (N; 21% O_2) or sustained hypoxia (H; 9% O_2) for 21
707 days. **a**, Hippocampal brain slices stained for IBA1. The quantification of the total number of
708 IBA1 reactive ($^+$) microglia is shown in the right bar graph (*n* = 3 –WT, N– or 4 –other groups–;
709 Student's *t*-test, two-sided). **b**, Relative levels of *Iba1* and *Gfap* mRNA in the hippocampus of N
710 and H *APP-PSEN1/+* mice. *Gapdh* mRNA was used as housekeeping control (*n* = 4 mice per
711 group; Student's *t*-test, two-sided). **c**, Hippocampal (Hp; left) and cortical (Cx; right) sections
712 stained with IBA1 (brown) and Thio-S (blue) or Tomato Lectin (TL; red) and Thio-S (green). **d**,
713 Quantification of the number of $IBA1^+$ microglial cells per Aß plaque (left graph; *n* = 5 mice;
714 Student's *t*-test, two-sided) and the percentage of area of individual Aß plaque occupied by
715 $IBA1^+$ microglia (right graph; *n* = 7 Hp/N, 8 Hp/H and Cx/N, or 9 Cx/H mice; Student's *t*-test,
716 two-sided). **e**, Representative images of hippocampal (left panels) and cortical (right panels)
717 sections stained for Ki67 (brown, phase contrast) and IBA1 (red), and counterstained with Thio-
718 S (green). Arrowheads indicate $Ki67^+$ microglia and insets depict the magnification of dotted
719 squares. Scale bars are 50 µm in low magnification panels and 25 µm in the insets. The right
720 graph shows the quantification of the density of $Ki67^+$ microglial cells (*n* = 9 mice per group;
721 Student's *t*-test, two-sided).
722 Data are presented in all the graphs as mean ± S.E.M. *n* are biological independent
723 experiments.
724 **Fig. 7 | Systemic sustained hypoxia enhances Aß aggregation, spreading, and Aß plaque-**
725 **associated axonal dystrophy. a–k**, 14-month-old *APP-PSEN1/+* mice were exposed to

normoxia (N; 21% O_2) or sustained hypoxia (N; 9% O_2) for 21 days. **a**, Brain sections were stained with Thio-S. **b**, Thio-S load (left graph) and plaque density (right graph) in N and H (*n* = 8; 4 mice per group. Student's *t*-test, two-sided). **c**, Size distribution of Thioflavin-S (Thio-S) plaques in N and H (*n* = 8; 4 mice per group; Student's *t*-test, two-sided). **d**, Brain sections stained for Aß. **e**, Aß load (left) and plaque density (right) were estimated from brain slices from N and H (*n* = 12; 4 mice per group; Student's *t*-test, two-sided). **f**, Size distribution of Aß plaques in N and H (*n* = 12; 4 mice per group; Student's *t*-test, two-sided). **g**, $Aß_{1-42}$ levels were quantified by ELISA in soluble brain extracts from N and H (*n* = 4 mice per group; Student's *t*-test; two-sided). **h**, Fibrillar Aß was detected by dot blot in soluble cortical extracts from N and H (*n* = 4 mice per group; a reference WT sample is shown). **i**, Cortical sections stained for ubiquitin (UB; right panels) and counterstained with Thio-S (left panels) in N and H. Right graph shows the quantification of the percentage of total UB load per slice in N and H (*n* = 8; 4 mice per group; Student's *t*-test, two-sided). **j**, Cortical sections stained with Thio-S (left panels) and for phospho-TAU (p-TAU; right panels) in N and H. Right graph shows the quantification of the percentage of individual Aß plaque area occupied by p-TAU+ neurites in N and H (*n* is indicated between brackets; Student's *t*-test, two-sided). **k**, *Sst* and *Npy* mRNAs levels were estimated by qRT-PCR in hippocampal extracts from normoxic (N: grey bars) and hypoxic (H: blue bars) *APP-PSEN1/+* mice. *Gapdh* mRNA was used as housekeeping control (*n* = 4; * $p < 0.05$ Student's *t*-test, two-sided).

Data are presented in all the graphs as mean ± S.E.M. *n* are biological independent experiments.

Fig. 8 | A human hypoxia-prone brain area contains nude Aß plaques with increased local axonal dystrophy. a, Fragments/kilobase of *HIF1a* per million mapped reads in human brain cells (http://www.brainrnaseq.org/[43]). FA: fetal astrocytes; MA: adult astrocytes; N: neurons; O: oligodendrocytes; M: microglia/macrophages; E: endothelial cells. **b**, Left, *HIF1A* qRT-PCR of human hippocampus from control (C; Braak I) and Braak and Braak stages II (ADII), III-IV (ADIII-IV), and V-VI (ADV-VI) subjects. Dots represent individual values (*n* is indicated between brackets; Kruskal-Wallis' test; $F = 7.124$; *GAPDH* control). Centre, HIF1α in protein extracts from human hippocampus (ß-actin control). Protein extract from HeLa cells in hypoxia (1% O_2, 4 h) as HIF1α control (right). Right, box and whisker graph show HIF1α/ß-actin levels (*n* is

indicated between brackets; *F* = 15.78; Kruskal-Wallis' test). **c**, mRNA levels estimated by qRT-PCR of human hippocampal samples (**b**) (*n* is indicated between brackets; Mann-Whitney U's test; *VEGFA*: *F* = 32; *HMOX*: *F* = 28; *SLC7A5*: *F* = 45; *BHLHE40*: *F* = 20; and *PRELID2*: *F* = 173). **d**, Left, staining of microglial cells (IBA1; brown) and Aß plaques (dark blue) in dentate gyrus (DG) (hypoxia susceptible area) and perirhinal cortex (control brain area) of human AD brain (Braak V-VI individuals). Right, plaque periphery covered by IBA1+ microglia (*n* is indicated between brackets from 3 different AD individuals; Mann-Whitney U's test). **e**, Left, staining of microglial cells (IBA1, brown), p-TAU^{+} dystrophic neurites (AT8, magenta), and Aß plaques (dark blue) in the DG of human AD brain (Braak V-VI). Right: axonal dystrophies (AT8 reactive) and Aß plaque area in samples with a protection index (IBA1^{+} area/individual Aß$^{+}$ plaques area ratio) lower or higher than 1. (*n* is indicated between brackets; Mann-Whitney U's test).

Data are presented in all the graphs as mean ± S.E.M. except in panel (**b**) (right), where the box represent the 25-75%, the central bar the median, and the error bar the maximal and the minimal values. *n* are biological independent experiments.

Human samples

Autopsy samples were obtained from the Neurological Tissue Bank of IDIBELL-Hospital of Bellvitge (Barcelona, Spain). The study (CEEA-US2017-13) was approved by the local ethics committee and by the "Comite de Etica de la Investigación (CEI), Hospital Virgen del Rocío", Seville, Spain. Samples with signed informed consent from "Banco de tejidos: Fundación CIEN (BT-CIEN; Centro de Investigación de Enfermedades Neurologicas; Madrid, Spain)" and from the Neurological Tissue Bank of IDIBELL-Hospital of Bellvitge (Barcelona, Spain), classified by Braak tau pathology (Supplementary Table 12).

Mice

Mice were housed under controlled temperature (22ºC) and humidity conditions in a 12 h light/dark cycle with *ad libitum* access to food and water. Housing and treatments were performed according to the animal care guidelines of the European Community Council (86/60/EEC). All animal procedures were conformed under the Spanish law and approved with number 26/04/2016/064 ("Consejería de agricultura, pesca y desarrollo rural. Dirección general de la producción agrícola y ganadera"). Heterozygous B6.Cg-Tg(APPswe,PSEN1Δ9E)85Dbo/J (*APP-PSEN1*/+; stock number 34832-JAX), B6;C3-Tg(Prnp-MAPT*P301S)PS19Vle/J (*MAPT*.pP301S/+; stock number 008169), B6.129-Hif1a tm3Rsjo/J ($Hif1a^{Flox/Flox}$; stock number 007561), and B6.129S4(C)-VHL tm1Jae/J; ($Vhl^{Flox/Flox}$; stock number 012933) mice were obtained from Jackson Laboratories. B6.129-Cx3cr1 tm2.1(cre/ERT2)Jung/Orl (*Cx3cr1-Cre::ERT2*/+ mice) were obtained from EMMA. APP751SL/+ mice (Sanofi) were provided by Transgenic Alliance-IFFA-Credo. WT were C57/Bl6J. To activate Cre::ERT2-mediated recombination, mice were fed for 30 days with a tamoxifen diet (400 mg tamoxifen citrate/kg; Envigo). All experiments were performed with balanced number of male and female mice.

***In vivo* hypoxia treatment**

Mice (14-month-old) were chronically exposed to 9% O_2 using a specially designed hermetic chamber with O_2 and CO_2 controllers and temperature and humidity monitoring (Coy Laboratory Products, Inc., Grass Lake, MI). Light, feeding, and cleaning cycles were kept uniform for all groups. Normoxic mice (controls) were also exposed to the same chamber but under a 21% O_2.

BV2 cell line culture

802 The microglial cell line was obtained from the Interlab Cell Line Collection (National Institute for
803 Cancer Research and Advanced Biotechnology Center, Italy). Cells were grown in RPMI 1640
804 medium (PAA) with 10% FBS (Gibco), 2 mM L-glutamine (Gibco) and 1% penicillin/streptomycin
805 (Gibco) in a water-saturated atmosphere of 5% CO_2 and 5% air. Cells were detached by
806 trypsinization with 0.25% trypsin-EDTA (Gibco). Cells were always plated at 30%–50%
807 confluence to prevent anaerobic conditions and the activation of microglial cells.

808 **Primary microglial cell cultures**

809 Primary microglia cultures were prepared as previously described[7] from 1 to 3-day-old WT
810 or *Cx3cr1-Cre::ERT2; Hif1α* $^{Flox/Flox}$ mice brains.

811 ***In cellulo* treatments**

812 *Tamoxifen (TMX)*. Primary microglia cultures were treated with 100 nM TMX for 6 days before
813 microglia isolation by mild trypsinization. *DMOG*. Cells were incubated for 24 h in 1 or 0.1 mM
814 DMOG dissolved in DMSO. A Similar amount of DMSO was added to control cultures. *Hypoxia*,
815 hypoxic conditions (1% O_2, and 5% CO_2) were achieved in a humidified variable aerobic
816 workstation (Invivo2 300; Ruskinn). *siRNAs.* BV2 cells were transfected with siRNAs (20 nM) in
817 suspension at 60–70% confluence for 48 h, using Lipofectamine 2000 (Invitrogen) as a
818 transfection reagent following the manufacturer's instructions.

819 **Flow cytometry**

820 *Cell cycle analysis.* 1 x 10^6 BV2 cells were harvested, PBS washed and resuspended in 5 mL
821 of ice-cold 70% ethanol, and left overnight at 4ºC. Cells were resuspended in 700 µL of
822 FACS/EDTA (5 mM). Incubated at RT for 15 min, washed twice with 500 µL of FACS/EDTA,
823 and finally resuspended in 800 µL of of FACS/EDTA supplemented with 0.2 mg/mL of RNAse A
824 (Qiagen) and incubated at 37ºC in agitation for 1.5 h. Before analysis, 0.04 mg/mL of propidium
825 iodide (Calbiochem) was added and the samples were incubated at 4ºC for 15 min in the dark.
826 Cells were resuspended in 500 µL of FACS/EDTA. Flow cytometry was performed in a BD
827 LSRFortessaTM and cell cycle distribution was analyzed using BD FACSDivaTM
828 software. *Acute isolation of microglia from adult brain.* Isolated cells were stained with
829 antibodies CD11b-APC and CD45-PE at 4°C for 30 min. Staining with isotype control-PE and
830 isotype control-APC was used as a negative control. Both control and experimental samples
831 were incubated with anti-CD16/CD32 blocker simultaneously. Cells were washed and sorted

using a FACS Aria Fusion (Becton Dickinson) flow cytometer and data were acquired and analyzed with FACSDiva software 8.0 (Becton Dickinson). Gating strategy and data analysis were made according to guidelines[53]. To separate CLEC7a high and low populations, we used an anti-CD45-PE and an anti-CD11b-CFblue, with an anti-CLEC7a-FITC at RT for 20 min. Anti-CLEC7a-FMO control was included (cells stained with anti-CD45-PE and anti-CD11b-CFblue, but not with anti-CLEC7a-FITC) for autofluorescence values in the FITC channel.

RNA extraction and qRT-PCR

Primary cultures, FACS-isolated microglia, and mouse brain samples: RNA was extracted using TRIzol reagent (Life Technologies). RNA samples (0.8 µg for mouse cortical samples and 0.5 µg for primary cultured microglia) were treated with PerfeCTa DNase (Quanta Biosciences) and copied to cDNA using qScript cDNA Supermix (Quanta Biosciences). cDNA from FACS-isolated RNA microglia was amplified following the protocol in the microarray section. Real-time qRT-PCR was performed for all samples in a ViiA 7 Real-Time PCR System (Applied-Biosystems) using either Power SYBR-Green PCR Master Mix (Applied-Biosystems) or iTaq Universal Probes Supermix (Bio-Rad) (Supplementary Table 13). *Human samples*: Total RNA and proteins were extracted using TriPure Isolation Reagent (Roche). RNA integrity (RIN) was determined by RNA Nano 6000 (Agilent). No significant differences between Braak groups were observed (RIN = 4.95 ± 1.4). Retrotranscription using 4 µg of total RNA was performed with the High-Capacity cDNA Archive Kit (Applied Biosystems). 40 ng of cDNA were mixed with 2x Taqman Universal Master Mix (Applied Biosystems) and 20× Taqman Gene Expression assay probes (Applied Biosystems) in an ABI Prism 7900HT (Applied Biosystems).

Microarrays

RNA quality was assessed using Agilent 2100 Bioanalyzer (threshold: RIN > 7). RNA Amplification, cDNA hybridization and array scanning were performed using GeneChip® WT Pico Reagent Kit, Mouse Transcriptome 1.0 Array and Scanner 3000 Affymetrix. Raw data from Expression Console software (Affymetrix) were exported to R-environment using LIMMA/Bioconductor packages (RStudio, Inc.). Quality assessment, data normalization and differential expression analysis were performed using Array Quality Metrics package, Robust Multi-Array method and LIMMA/Bioconductor package respectively. Data is available at Gene Expression Omnibus repository. Gene expression data from *5xfAD*, *APP751SL/+*,

862 *MAPT*p.P301S/+, Amyotrophic lateral sclerosis, and aged mouse models were analysed with
863 the Gene Set Enrichment Analysis (GSEA) using Biological Processes C5-v5.2, KEGG and the
864 custom HIF1/hypoxia-induced microglial module (HMM), mTOR, and Microglial
865 neurodegenerative phenotype (MGnD) GSs.

866 **Protein extraction and western blot**

867 *Primary cultures*. Total proteins were extracted using TRIzol reagent (Life Technologies)
868 according to the manufacturer's instructions. Blotting for HIF1α, samples were resuspended in
869 lysis buffer 1 (30 mM Tris-HCl, 2 M thiourea, 7 M urea, 4% (w/v) CHAPS pH 8.5). RC-DC
870 protein assay kit (Bio-Rad) was used for quantifications. *Human samples*. Proteins were
871 obtained from frozen human hippocampal tissue after sequential RNA and DNA extraction using
872 TripureTM Isolation Reagent (Roche). Protein pellets were solubilized using 4% (w/v) SDS, 8 M
873 urea, 40 mM Tris-HCl, pH 7.4 under rotation overnight at RT and quantified by Lowry assay.
874 Western blots were performed using standard procedures. Antibodies used were anti-HIF1α
875 (1:100), anti-NDUFS2 (1:1,000), anti-SDHA (1:1,000), anti-ATPsynß (1:1,000), anti-RPL26
876 (1:1,000), and anti-ß-actin (1:5,000). HRP-conjugated anti-rabbit (1:10,000) or anti-mouse
877 (1:10,000) antibodies and Western ECL Substrate kit (Bio-Rad) were used for signal
878 detection.

879 **Immunodetection**

880 *In cellulo.* Microglial cultures plated on coverslips were stained under standard protocols with
881 anti-IBA1 and anti-GFAP to detect astrocyte contamination. Images were taken with a BX-61
882 microscope (Olympus). *BrdU staining*; cultures were incubated (3 h) in a media containing 10
883 µM BrdU (Sigma). Cells were fixed with ice-cold 4% paraformaldehyde for 10 min and
884 permeabilized with ice-cold 70% ethanol at 4ºC overnight. Samples were treated with 2 M HCl
885 for 15 min to denature the DNA followed by incubation with 0.1 M sodium borate pH 6.8 for 15
886 min. *Mice*. The brain was removed from perfused mice with PBS and immediately fixed
887 overnight (15 h) at 4°C with 4% PFA in PBS. The brain was paraffin-embedded using an
888 automatic tissue processor (ASP300S, Leica) and paraffin blocks cut in 20 µm thick coronal
889 sections using a microtome (RM2255, Leica). Immunostaining was performed according to
890 standard protocols. Primary antibodies used: anti-IBA1 (1:500), anti-GFAP (1:1,000), anti-GS
891 (1:1,000), anti-UB (1:400), anti-Aß 6e10 (1:500), anti-NDUFS2 (1:1,000), anti-Ki67 (1:200), and

anti-p-TAU (1:500). For immunohistochemistry, Envision+ kit (DAKO) was used for chromatic staining. Secondary antibodies were added the reaction was developed with 3,3-diaminobenzidine (DAB, DAKO). For immunofluorescent studies, we used secondary antibodies anti-mouse or anti-rabbit conjugated with Alexa-488 or Alexa-568. Tomato lectin staining was performed incubating sections at 37ºC for 1 h, followed by incubation with Cy3-conjugated streptavidin (1:500). Thioflavin-S, DAPI, and Prussian blue staining were used as counterstains. *Human*. For double labeling light microscopy, sections were incubated with the microglial marker (anti-IBA1, 1:1,000), followed by the biotinylated secondary antibody and streptavidin-conjugated horseradish peroxidase. The peroxidase reaction was visualized with 0.05% 3-3-diaminobenzidine tetrahydrochloride (DAB, Sigma-Aldrich), 0.03% nickel ammonium sulfate, and 0.01% hydrogen peroxide in PBS. After the DAB-nickel reaction (dark blue end product), sections were then incubated with the anti-Aß antibody (1:2,000). The second immunoperoxidase reaction was developed with DAB only (brown reaction end product). For triple immunolabeling, dark blue (anti-Aβ) and brown (anti-IBA1)-peroxidase reactions were sequentially developed. Sections were then incubated with the p-TAU antibody (1:500) and visualized using the VECTOR® VIP Peroxidase Substrate Kit (Vector Laboratories). Sections were then mounted on gelatin-coated slides, air-dried, dehydrated in graded ethanol, cleared in xylene, and coverslipped with DPX (BDH) mounting medium.

***In situ* hybridization and immunostaining**

Brain tissues were cryoprotected in sucrose, embedded in OCT compound (Tissue-Tek), and kept at –80 °C. 10 µm coronal slices were obtained with a cryostat (Leica). RNAscope 2.5 (ACD) protocol was used to detect *Hif1a* mRNA (ACD) according to the manufacturer's instructions, using a HybEZ oven (ACD). Subsequent immunostaining was performed for microglia staining (with IBA1 marker) and nuclear staining (DAPI dye). After RNAscope 2.5 protocol, slices were incubated for 10 min in PBS-Triton X100 0.3 % (v/v) and washed in PBS. Samples were incubated with anti-IBA1 antibody (1:500) O/N at 4 °C. Slices were then incubated with Alexa 488 anti-rabbit (1:400) for 1 h at RT and DAPI (Sigma, 1:1,000) stained before mounting with Fluoromount-G. Images were acquired in a confocal microscope (Nikon A1R+).

Electron microscopy

Mice brains were processed according to standard protocols for electron microscopy visualization. Selected areas were cut in ultrathin sections, stained with uranyl acetate and lead citrate, and examined with an electron microscope (JEOL JEM 1400). Quantification of mitochondrial morphology was performed in Fiji by measuring area, perimeter, and major and minor axis. The "Fit Ellipse" function was used to calculate the major and minor axes. The following parameters were calculated: (i) Circularity: 4π*area/perimeter^2. A value of 1.0 indicates a perfect circle. As the value approaches 0.0, it indicates an increasingly elongated shape. (ii) Aspect ratio: major axis/minor axes.

Bioenergetic analysis of primary microglial cell cultures

Seahorse Extracellular Flux (XFp) Analyzer (Agilent Seahorse). Primary microglial cells (3.5 x 10^4 cells/well) were seeded (80 µl/well) in XFp cell culture mini plates and incubated at 37°C in a humidified incubator with 5% CO_2 for 24 h in their cell growth medium. For the mitochondrial stress test, oligomycin (20 µM) carbonyl cyanide-p-trifluoromethoxyphenylhydrazone (FCCP; 20 µM) and rotenone/antimycin A (10 µM; all Agilent Seahorse) were loaded for sequential delivery. For the glycolytic rate assay test, rotenone/antimycin A (10 µM) and 2-deoxy-D-glucose (2-DG; 500 mM; all Agilent Seahorse) were similarly loaded. Following calibration, oxygen consumption rate (OCR), extracellular acidification rate (ECAR), and proton efflux rate (PER) were measured every 6 min for 72 min and the compounds were injected sequentially at 18 min intervals. OCR, ECAR, and PER were automatically calculated using Seahorse XFp software and 4–6 biological independent replicates were assessed for each condition.

Microglial coverage and stereological quantification

Human periplaque coverage. The periplaque microglial coverage was defined as the percentage of area stained with IBA1 in the periplaque area (delimited by drawing a circle 30 µm from the plaque edge). Images of IBA1/4G8 stained sections were acquired using the automated digital microscopy system (Olympus VS120, Denmark) connected to an Olympus BX61VS with a high-resolution digital color camera (VC50 Olympus). Images from plaques of the different brain areas (dentate gyrus and perirhinal cortex) were then acquired using the Olyvia 2.6 image viewer software (Olympus, Denmark) (image size: 1654 pixel x 877 pixel; pixel size: 28.34 pixel/cm). Digital images (n = 3 individuals Braak V-VI) were processed using the Visilog 6.3 (Noesis, France) image analysis system. *Dystrophy pathology related to microglial*

coverage was quantified per each plaque analyzing the percentages of area stained with AT8 (p-TAU) and with IBA1 in the plaque area. Images of AT8/IBA1/4G8 triple immunostained sections from dentate gyrus were acquired using the digital microscopy system (Olympus VS120) as described for periplaque coverage quantification. Digital images were processed using Fiji (ImageJ). Three different binary masks (AT8, IBA1, and 4G8-reactive area) were generated using the color threshold segmentation (HSB mode) and each selected area was measured. Finally, the protection index was calculated as the ratio IBA1/Aβ plaque. *Number, coverage of mouse Aß plaques, and proliferative microglia*. Amyloid plaques were visualized with Thio-S staining and were randomly selected blind to the treatment in the cortex and hippocampus. Quantifications were done in superimages generated with the NewCAST system (Visiopharm) associated with the microscope BX61 (Olympus). The number of microglia cells surrounding amyloid plaques was determined after immunostaining for IBA1 and staining with DAPI using immunofluorescence. Microglia coverage of individual amyloid plaques was obtained by normalizing IBA1 occupied area by the area occupied for the corresponding Thio-S reactive plaque, calculated from binary masks generated with appropriate thresholds for all images in Fiji. Results are presented as a percentage of IBA1 per Aß plaque area. Proliferative microglia were identified as double reactive for Ki67 and IBA1. To quantify different signals around Aß plaques, we drawn a 50 µm radius circle and quantify the density using Fiji (ISH *Hif1a* mRNA and NDUFS2). In wild-type and regions distal to Aß plaques, full images were quantified and a density of the marker was calculated. *Microglial stereology*. The measurements were performed blind to the treatment. Unbiased stereological approach using an Olympus BX61 microscope combined with the CAST system. The sample area was then manually outlined and the total area quantified using CAST software and microglia between two specific bregma points were estimated using a dissector area of 28,521.3 µm2 (CAST). The dentate gyrus was chosen as a sample area.

Amyloid plaque quantification

These measurements were blind to the treatment. Quantifications were done in superimages generated with the NewCAST system (Visiopharm) associated with the microscope BX61 (Olympus). *Load.* The Thio-S and Aß plaques load were estimated using Fiji. A segmented binary mask was generated and the occupied area by detected particles over a specific

constant threshold was quantified. The load was defined as the percentage of total cortex area occupied by Thio-S and Aß. *Density*. This parameter was calculated by dividing the number of detected particles obtained in parallel to the load quantification described above by the sampled cortical area. *Frequency*. The size of each detected particle obtained with the load quantification above was registered and density was calculated for different intervals of plaque size.

Dystrophic neurites quantification

Amyloid plaques were visualized upon Thio-S staining. These measurements were blind to the treatment. Quantifications were done in superimages generated with the NewCAST system (Visiopharm) associated with the microscope BX61 (Olympus). *Ubiquitin (UB) load.* The UB load was estimated using Fiji. A segmented binary mask was generated and the occupied area by detected particles over a specific constant threshold was quantified. The load was defined as the percentage of cortical brain area occupied by UB. *p-TAU load.* Plaques were randomly selected by Thio-S staining and the Thio-S and p-TAU area were estimated using Fiji in individual plaques. Results are presented as a percentage of p-TAU area per amyloid plaque area.

Aß ELISA

For soluble $A\beta_{1-42}$ quantification, proteins were extracted from acutely dissected hemibrains of using a Dounce's homogenizer in PBS (8x wet weight/volume buffer) containing phosphatase and protease inhibitors (Sigma, 1:1,000). Samples were consecutively centrifuged at 600 g, 15,000, and 100,000 g in an Optima-Max ultracentrifuge (Beckman-Coulter) at 4ºC. The supernatant was carefully decanted and stored on ice until used for the assay. For standard curve samples, lyophilized $A\beta_{1-42}$ synthetic peptide (Anaspec) was used. Human $A\beta_{1-42}$ ELISA Kit (Invitrogen) was used following the manufacturer's instructions. Measurements were normalized by protein levels using RC-DC protein assay kit (Bio-Rad).

Dot Blot

Cortical soluble extracts were obtained as described for soluble Aß quantification. Total protein was quantified with RC-DC kit (Biorad), according to manufacturer's guidelines, and using bovine serum albumin (BSA) for the standard curve. 1 µg of each soluble extract was spotted onto a nitrocellulose membrane (GE Healthcare) and air-dried for 30 min. The membrane was incubated ON with the primary antibody OC (Millipore, 1:5,000). Signal detection was performed

using a secondary HRP-conjugated anti-rabbit antibody and Western ECL Substrate kit (Bio-Rad).

List of abbreviations

AD: Alzheimer's disease; DAM: Disease-associated microglia; TREM2: Triggering receptor expressed on myeloid cells 2; APOE: Apolipoprotein E; MGnD: Microglial neurodegenerative phenotype; mTOR: Mechanistic/mammalian target of rapamycin; HIF1: Hypoxia-Inducible factor 1; AßAM: Aß plaque-associated microglia; ISH: *In situ* hybridization; TFEA: Transcription factor enrichment analysis; HMM: HIF1/hypoxia-induced microglial module; DE: Differentially expressed; ES: End-stage; WT: Wild-type; GSEA: Gene set enrichment analysis; OXPHOS: Oxidative phosphorylation; H: Hypoxia; N: Normoxia; R: Reoxygeneation; D: DMOG; PI: Propidium iodide; BrdU: Bromodeoxyuridine; oAß: Oligomeric Aß; PFA: Paraformaldehyde; ON: Overnight; RT: Room temperature.

Statistical analysis

All individual measurements constitute biological replicates. Samples with an $n < 9$ were analyzed using parametric tests. Samples with an $n \geq 9$ were evaluated for normal distribution using D'Agostino and Pearson's omnibus normality test. Comparisons between two groups were performed with two-sided unpaired Student's *t*-test whereas comparisons between more than two groups were done with ANOVA with Tukey's test. Data are expressed as mean ± standard error of the mean (S.E.M.) at less specified in the figure legends; $p \leq 0.05$ was considered statistically significant. For human samples, different groups were compared using Mann-Whitney U's test. Statistical analyses and graphs were performed in GraphPad Prism version 9.0 (GraphPad Inc.).

Data availability

The raw data are available at the Source Data accompanying this article. Transcriptomics data are available at GEO with the following accession numbers: (i) Mouse primary microglial cultures exposed to normoxia or hypoxia: GSE97423; (ii) Isolated Clec7a^{+} microglia from WT, *APP*$_{751}$*SL* and *MAPT*p.P301S mice: GSE129296; and (iii) Isolated microglia from *APP-PSEN1/+*; *VHL*$^{Flox/-}$ with or without TMX treatment GSE168059.

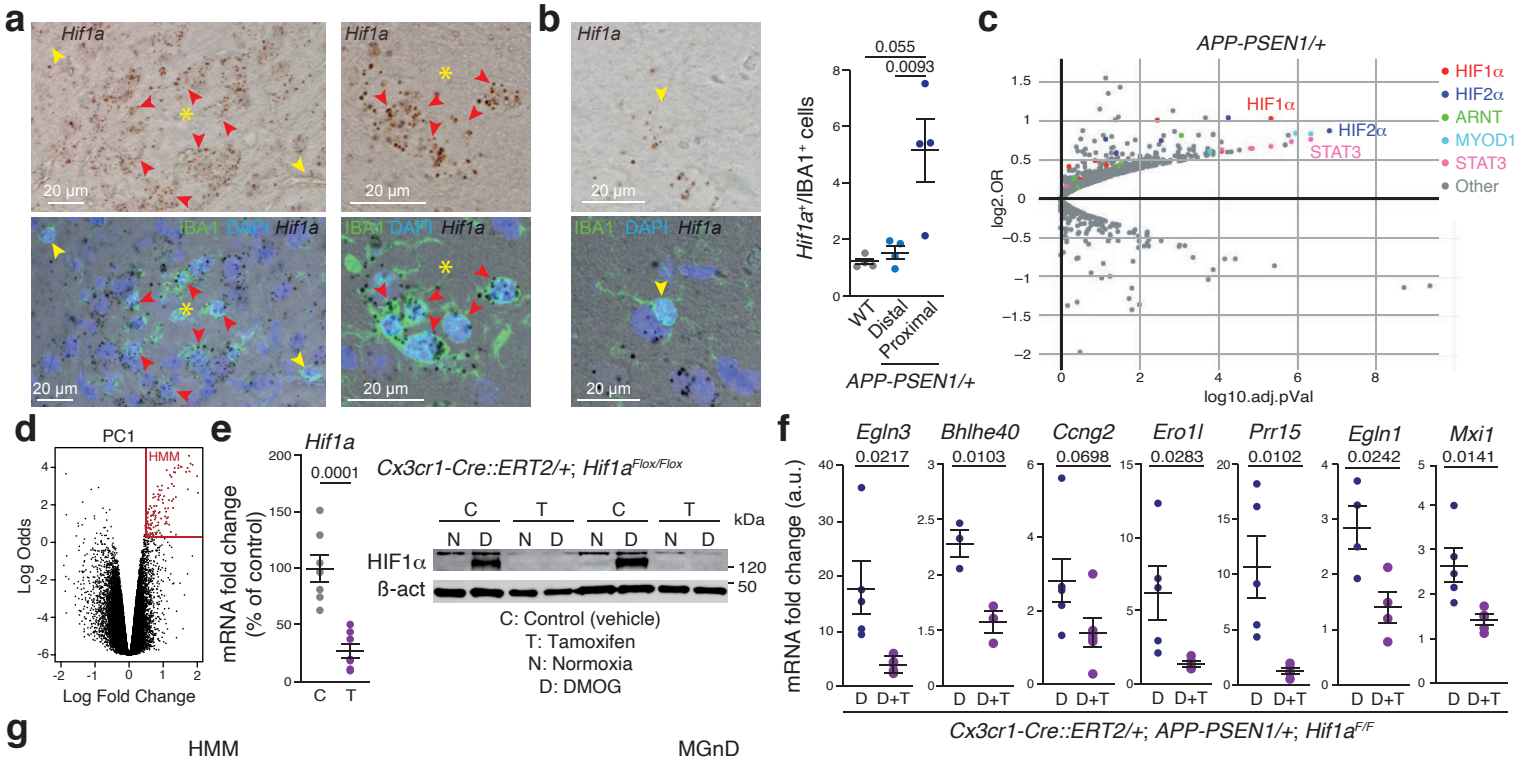

Gene sets enriched in *APP/+* pathologic state *vs* WT microglia

Name	NES	FWER-*p*-val
MGnD	2.74	0
GO_OXIDATIVE_PHOSPHORYLATION	2.63	0
GO_RESPONSE_TO_TYPE_I_INTERFERON	2.62	0
HMM	2.58	0
GO_ESTABLISHMENT_OF_PROTEIN_...	2.5	0
GO_ELECTRON_TRANSPORT_CHAIN	2.48	0
GO_RESPONSE_TO_VIRUS	2.45	0
GO_CELLULAR_RESPIRATION	2.42	0
GO_NEGATIVE_REGULATION_OF_VIRAL_...	2.42	0
GO_TRANSLATIONAL_TERMINATION	2.41	0
GO_NEGATIVE_REGULATION_OF_TUMOR_...	2.4	0
GO_TRANSLATIONAL_INITIATION	2.39	0.001
GO_DEFENSE_RESPONSE_TO_VIRUS	2.33	0.002
GO_MITOCHONDRIAL_RESPIRATORY_CHAIN...	2.31	0.002
GO_REGULATION_OF_MYELOID_CELL_...	2.31	0.003

March-Diaz *et al.*, Figure 1

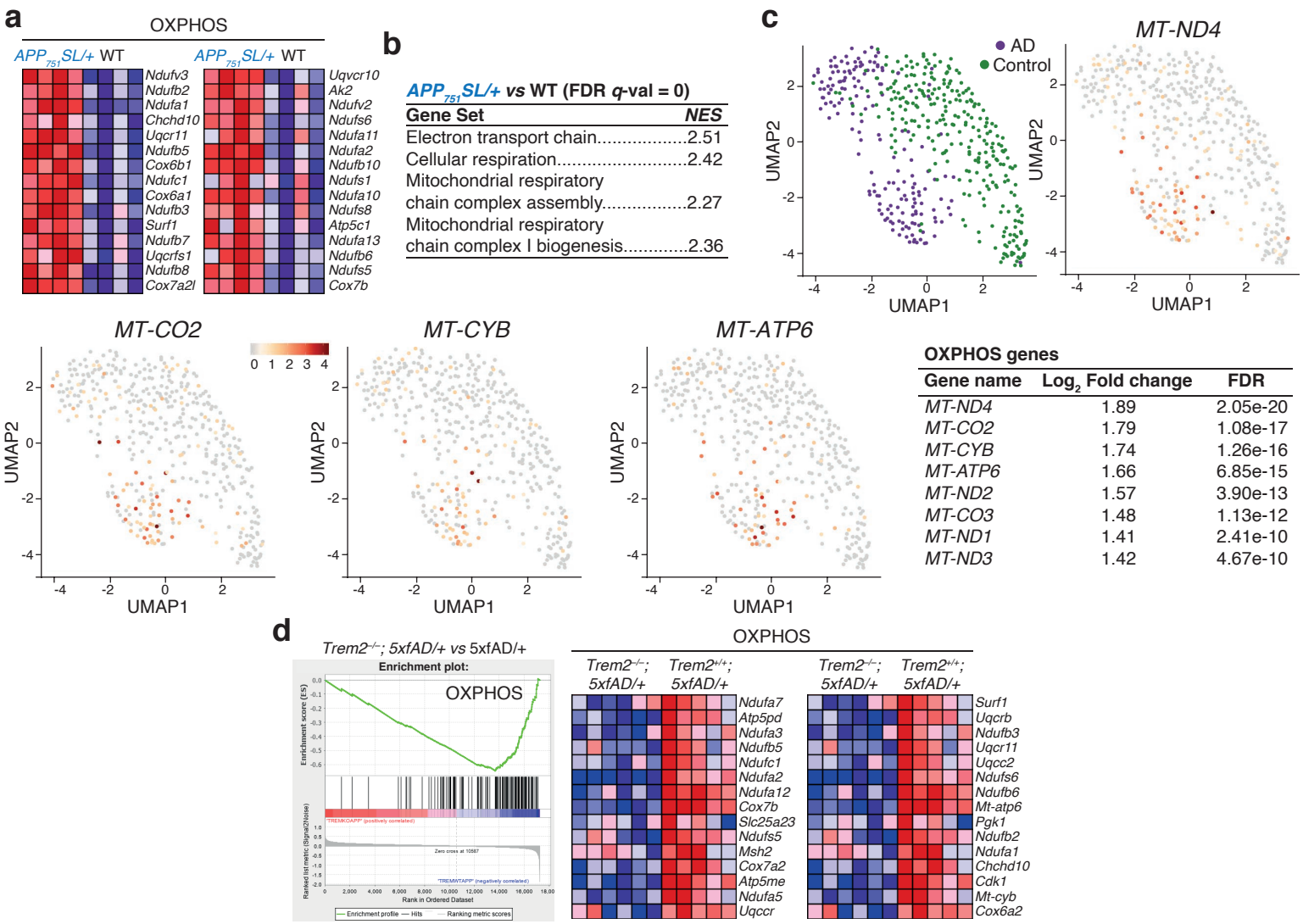

March-Diaz *et al.*, Figure 2

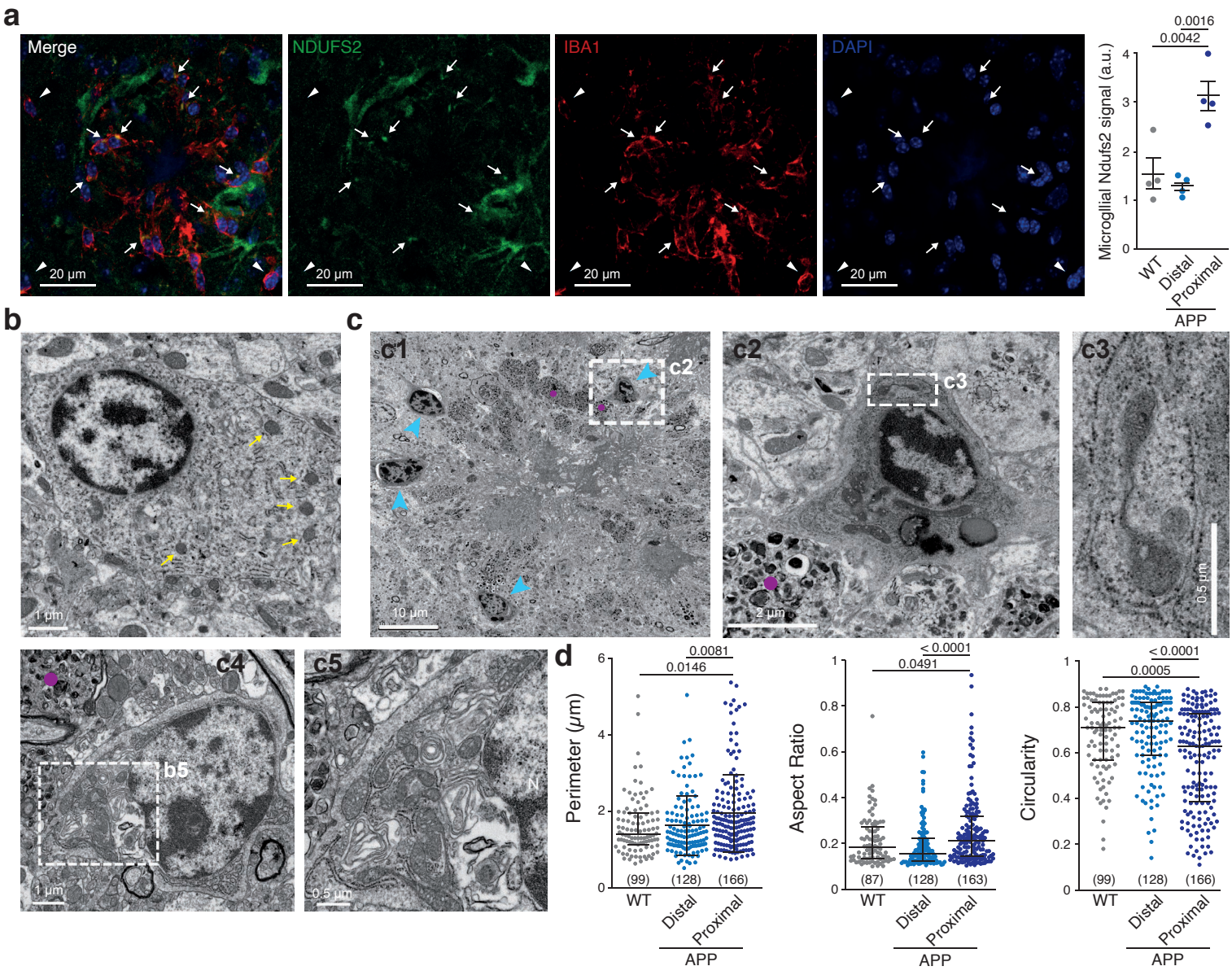

March-Diaz *et al.*, Figure 3

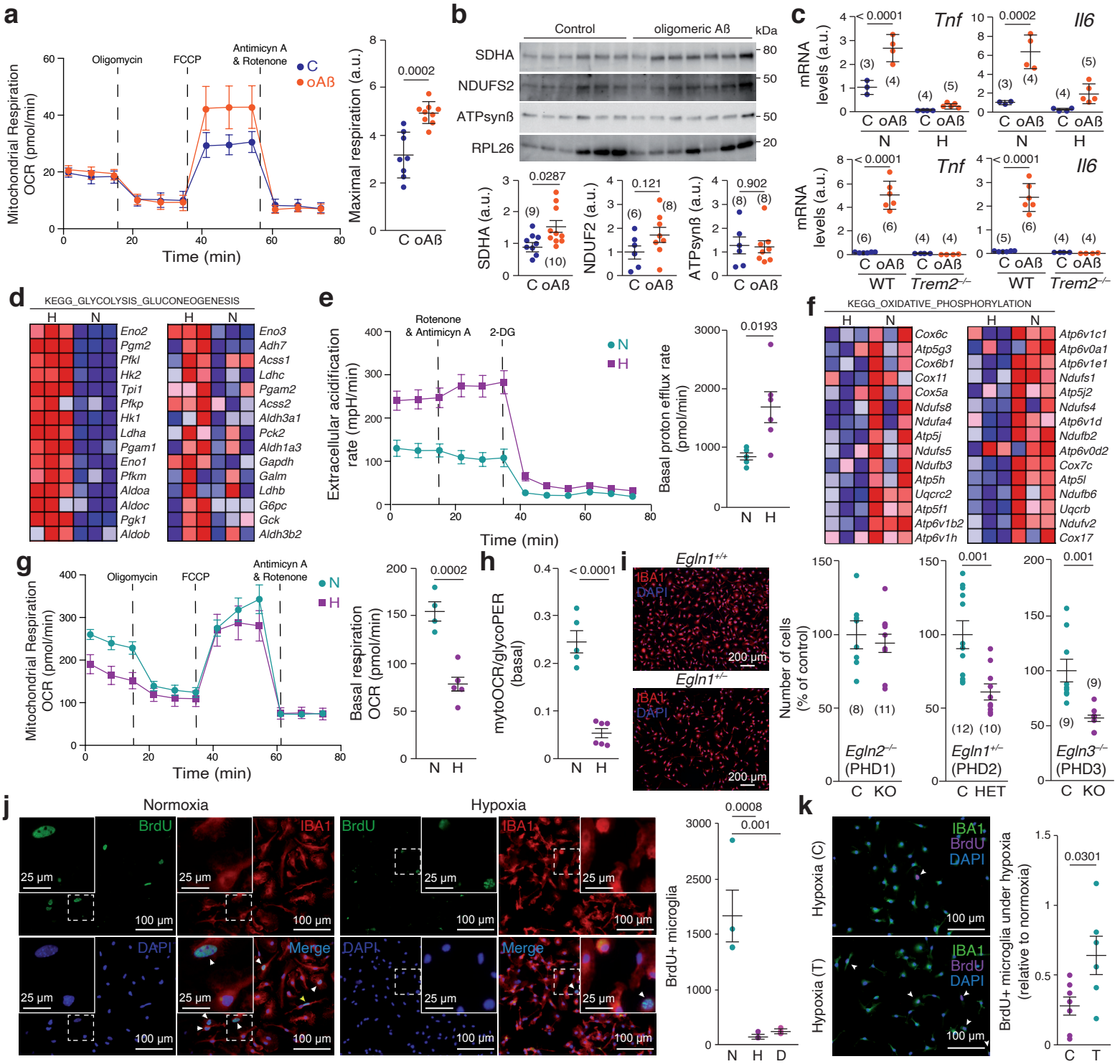

March-Diaz *et al.*, Figure 4

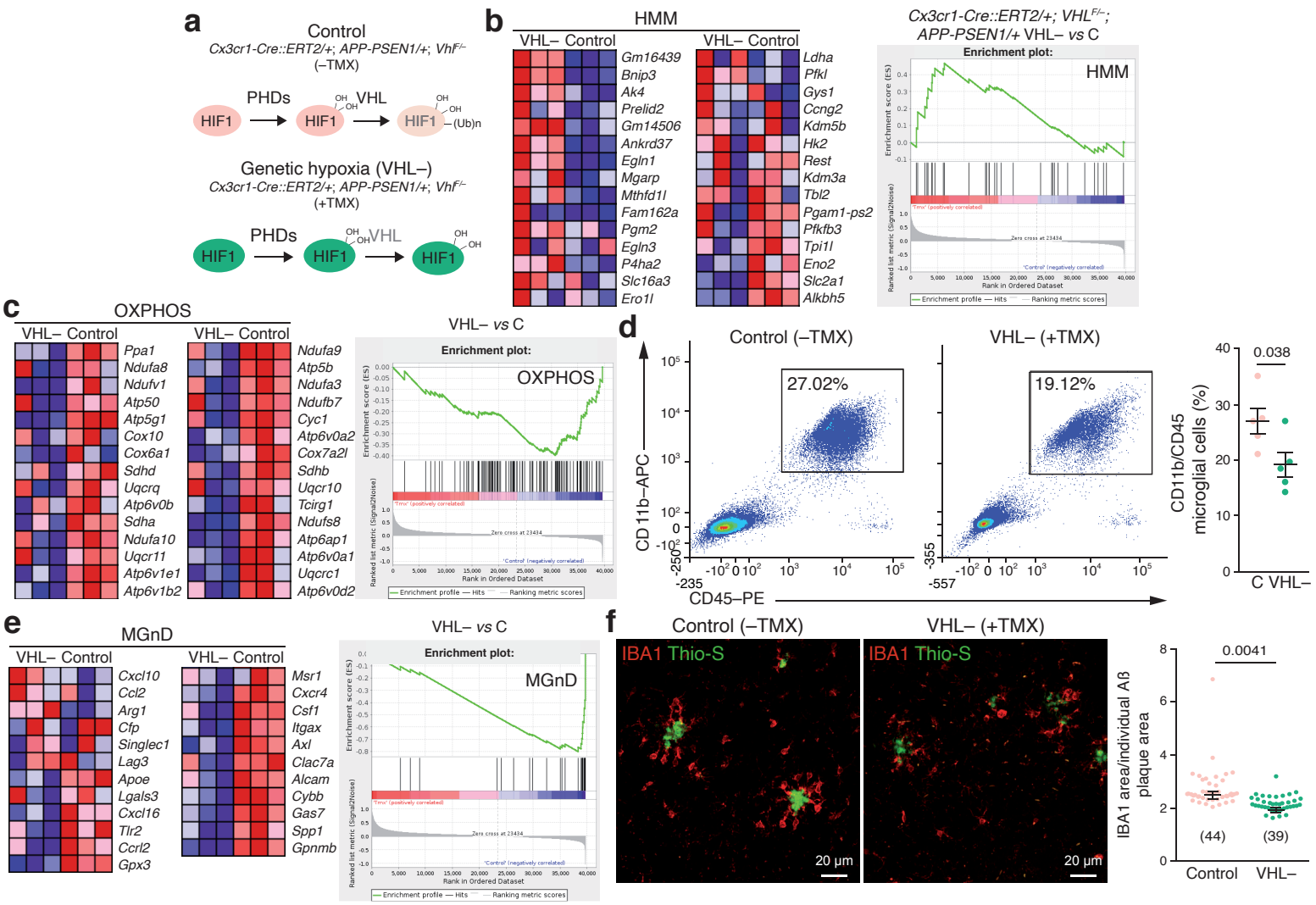

March-Diaz *et al.*, Figure 5

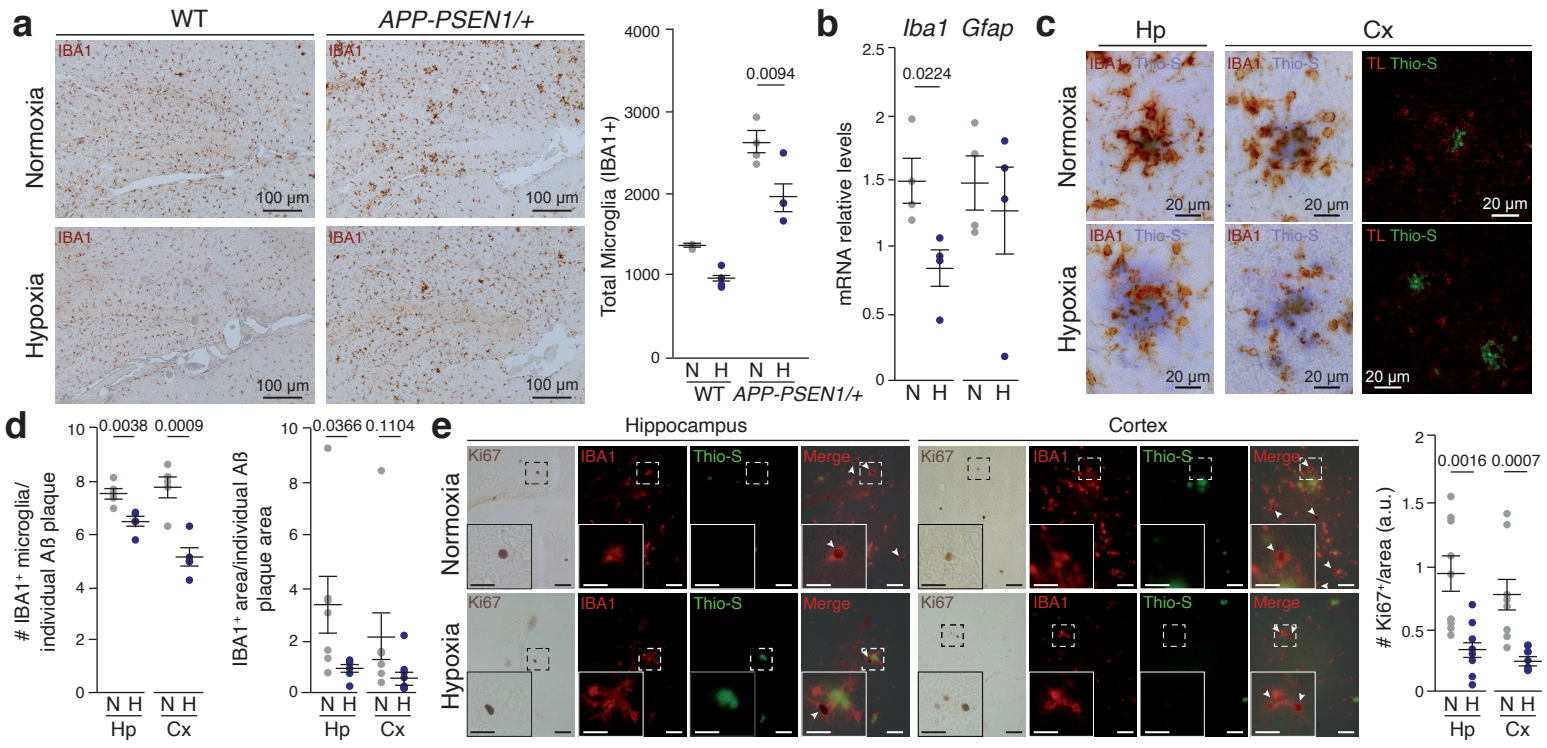

March-Diaz *et al.*, Figure 6

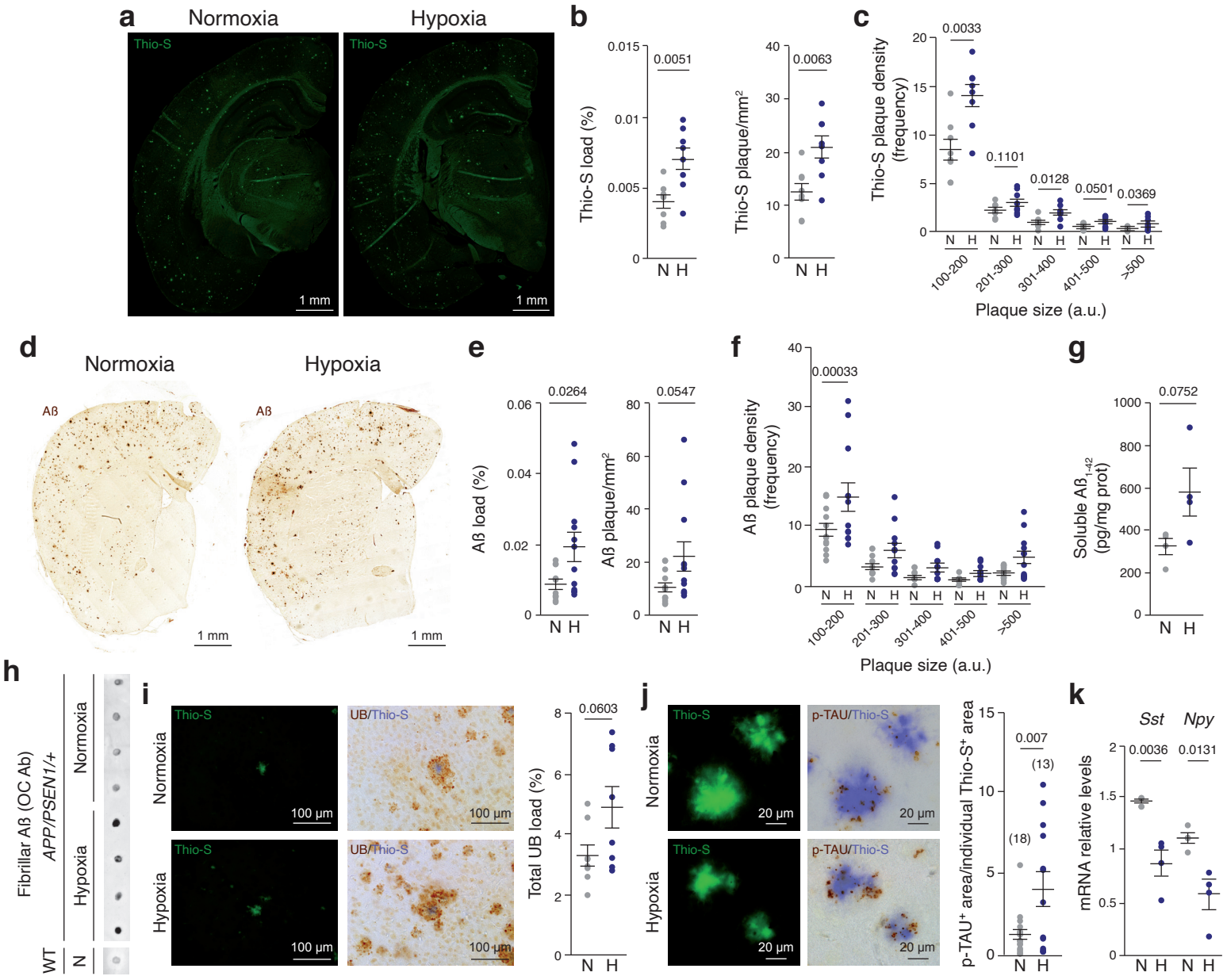

March-Diaz *et al.*, Figure 7

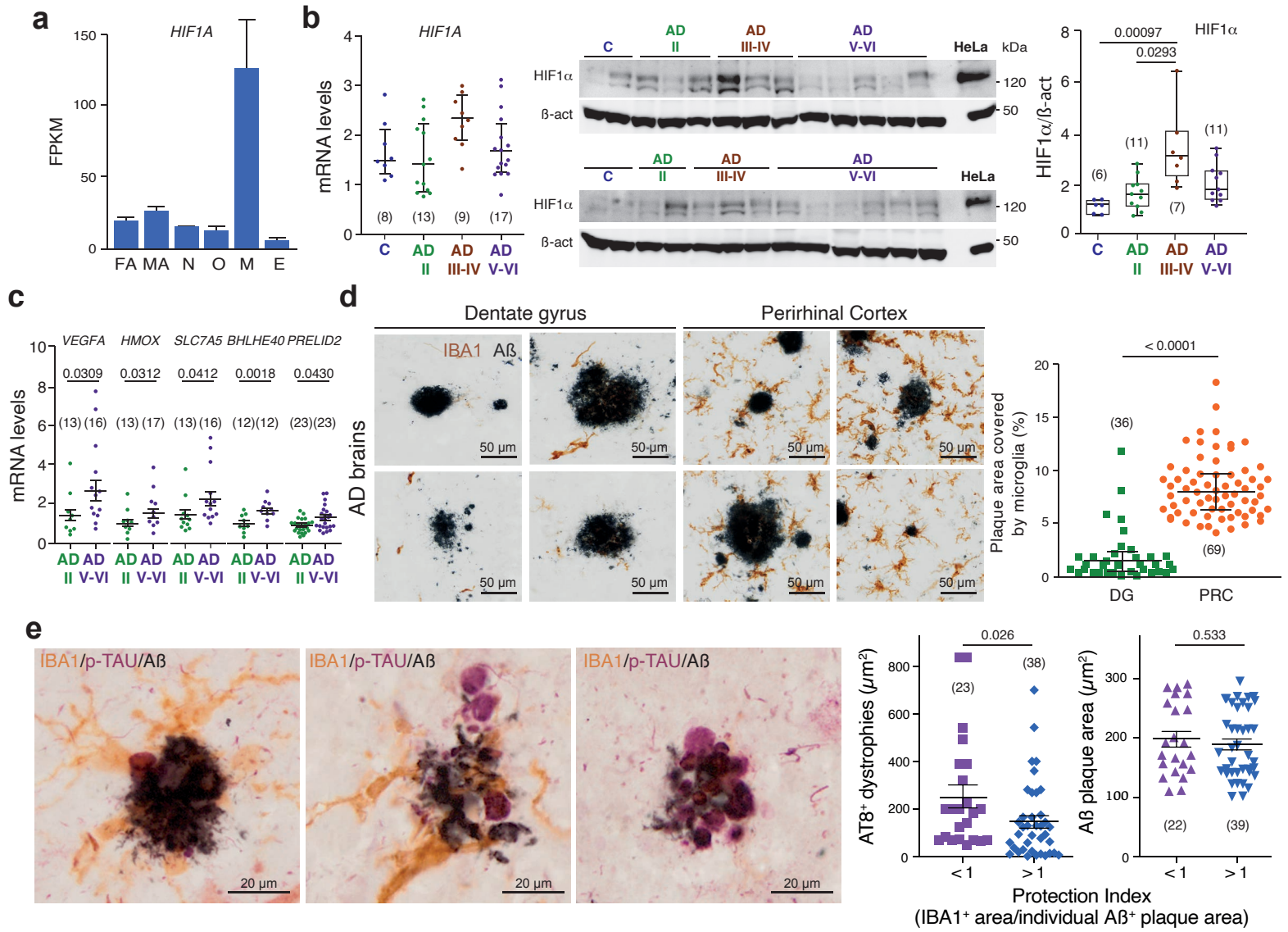

March-Diaz *et al.*, Figure 8